Journal of South American Earth Sciences 89 (2019) 275–298

Contents lists available at ScienceDirect

Journal of South American Earth Sciences

journal homepage: www.elsevier.com/locate/jsames

# Bauxite formation on Tertiary sediments in the coastal plain of Suriname

Dewany A. Monsels[a,*], Manfred J. Van Bergen[b]

[a] Department of Geology and Mining, Anton de Kom University of Suriname, Leysweg 86, Paramaribo, Suriname
[b] Department of Earth Sciences, Utrecht University Budapestlaan 4, 3584CD, Utrecht, the Netherlands

ARTICLE INFO

*Keywords:*
Lateritic bauxite
Tertiary sediments
Trace elements
Suriname

ABSTRACT

Lateritic bauxites in the coastal lowlands of Suriname form part of a belt along the northern margin of the Guiana Shield that has long been one of the world's major bauxite producing regions. The Surinamese deposits, many of which with an extensive mining history, originated on Tertiary siliciclastic sediments and were mostly buried under a layer of young sediments. The bauxite-bearing sequences are generally topped with an iron-rich layer largely made up of hematite and goethite. It covers a gibbsite-rich bauxite horizon that passes downward into a kaolinitic bottom section containing anatase and zircon as main accessory minerals. Weathering profiles across formerly mined deposits were analyzed for geochemical and mineralogical properties aimed at exploring compositional diversity, underlying controls of bauxite-formation and the nature of precursor sediments.

Studied profiles in different parts of the coastal plain reveal overall similarities between individual deposits in showing significant depletion of Si, K, Na, Mg and Ca and strong, primarily residual, relative enrichment of Al, Ti, Zr, Nb, Hf, Ta and Th. In detail, however, there are distinct differences in major and trace-element signatures, accessory mineral assemblages, facies distribution and provenance of the terrigenous precursor sediments. Enrichments in high field-strength elements and heavy rare earth elements are largely attributable to accumulation of heavy minerals like zircon in the precursor. Petrological and trace-element evidence does not support a direct genetic relationship between bauxite and the underlying saprolitic clays. The complex petrologic characteristics and compositional heterogeneity of the coastal-plain deposits can essentially be explained by element fractionation, primarily through selective leaching, in combination with relative and absolute enrichment processes, erosion and reworking during two-stage, polycyclic bauxitization of a heterogeneous precursor.

## 1. Introduction

Bauxite deposits in South America are all of lateritic affinity but developed on a variety of parent rocks (precursors) ranging from Phanerozoic siliciclastic sediments to Precambrian igneous and metamorphic lithologies (Bárdossy and Aleva, 1990; Carvalho et al., 1997; Bogatyrev et al., 2009). The most significant deposits, hosting some of the largest reserves worldwide, are distributed within and along the Precambrian Guiana Shield in northern Brazil (Amazon Basin and surroundings), Venezuela, Guyana, Suriname and French Guiana (Fig. 1a), where long-lasting tropical and highly humid conditions favored intense chemical weathering, and a tectonically stable environment further facilitated the formation of planation surfaces with extensive lateritic bauxite deposits.

The lateritic bauxites of Suriname are categorized into two major geographic areas (Fig. 1b) with different precursors, properties and exploitation histories (Bárdossy and Aleva, 1990; Aleva and Wong, 1998; Monsels, 2016). One group, referred to as "coastal-plain bauxites", formed on sedimentary parent material in the coastal lowlands and was mined since the early 20th century until recently, while the second group of "plateau bauxites" largely originated on various metamorphosed crystalline rocks of Proterozoic age in interior parts of the country (Monsels, 2016; Monsels and Van Bergen, 2017), and has not been exploited to date. Collectively, these lateritic bauxite deposits belong to a series of regional planation surfaces on the northern margin of the Guiana Shield and its sedimentary cover where bauxite developed intermittently from Late Cretaceous to Quaternary times, with the Early Tertiary as most productive interval (King et al., 1964; Bárdossy and Aleva, 1990; Théveniaut and Freyssinet, 2002) (Fig. 1a,c).

The bauxite deposits of economic interest in the coastal plain belong to the Paleocene-Eocene "Main Bauxite Level" or "Sul-Americano" planation level, formed on Late Cretaceous-Early Tertiary sedimentary parent material. They are often buried by Miocene and younger sediments as a result of marine transgressions (Van der Hammen and Wijmstra, 1964; Bárdossy and Aleva, 1990; Théveniaut and Freyssinet, 2002; Wong et al., 2009) (Fig. 1c). A so-called "Bauxite belt" runs subparallel to the Old Coastal Plain of Suriname and continues into

* Corresponding author.
*E-mail address:* dewany.monsels@uvs.edu (D.A. Monsels).

https://doi.org/10.1016/j.jsames.2018.10.010
Received 20 November 2017; Received in revised form 16 September 2018; Accepted 25 October 2018
Available online 30 October 2018
0895-9811/ 

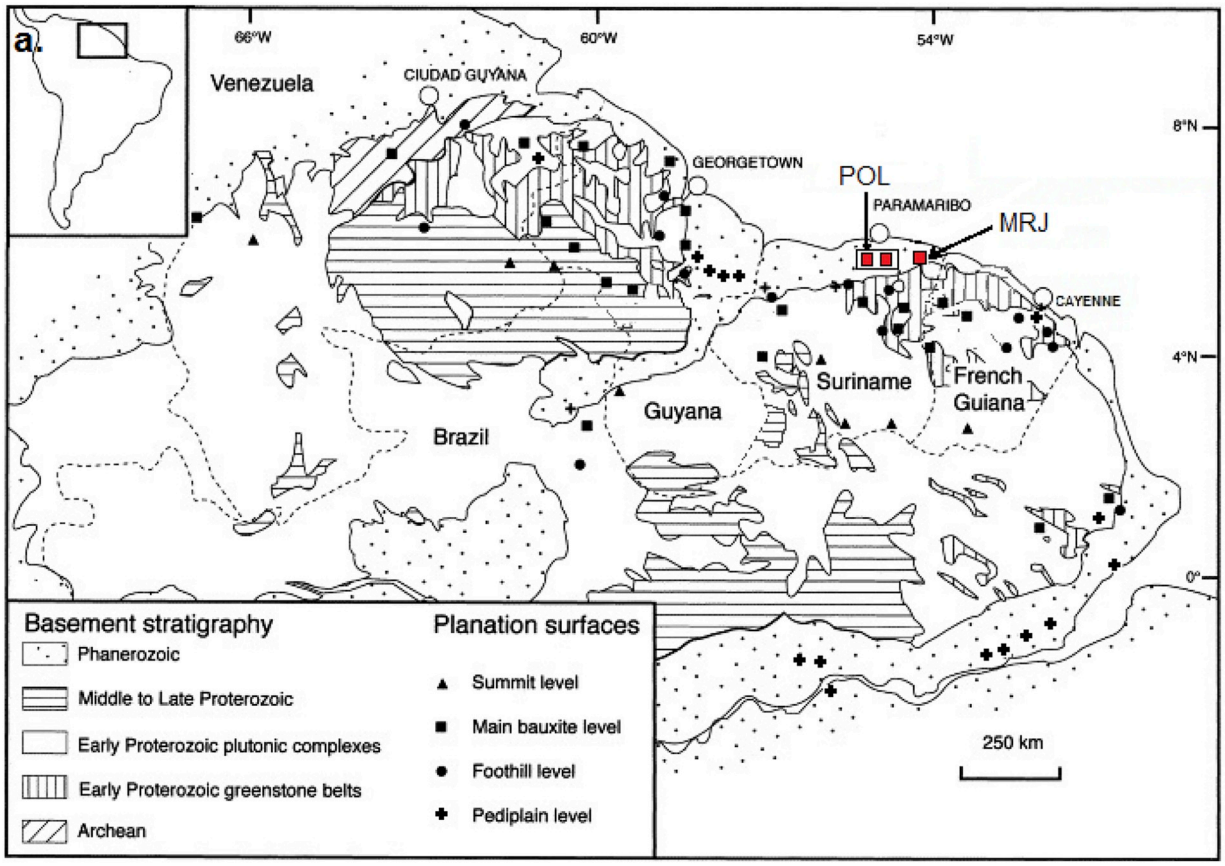


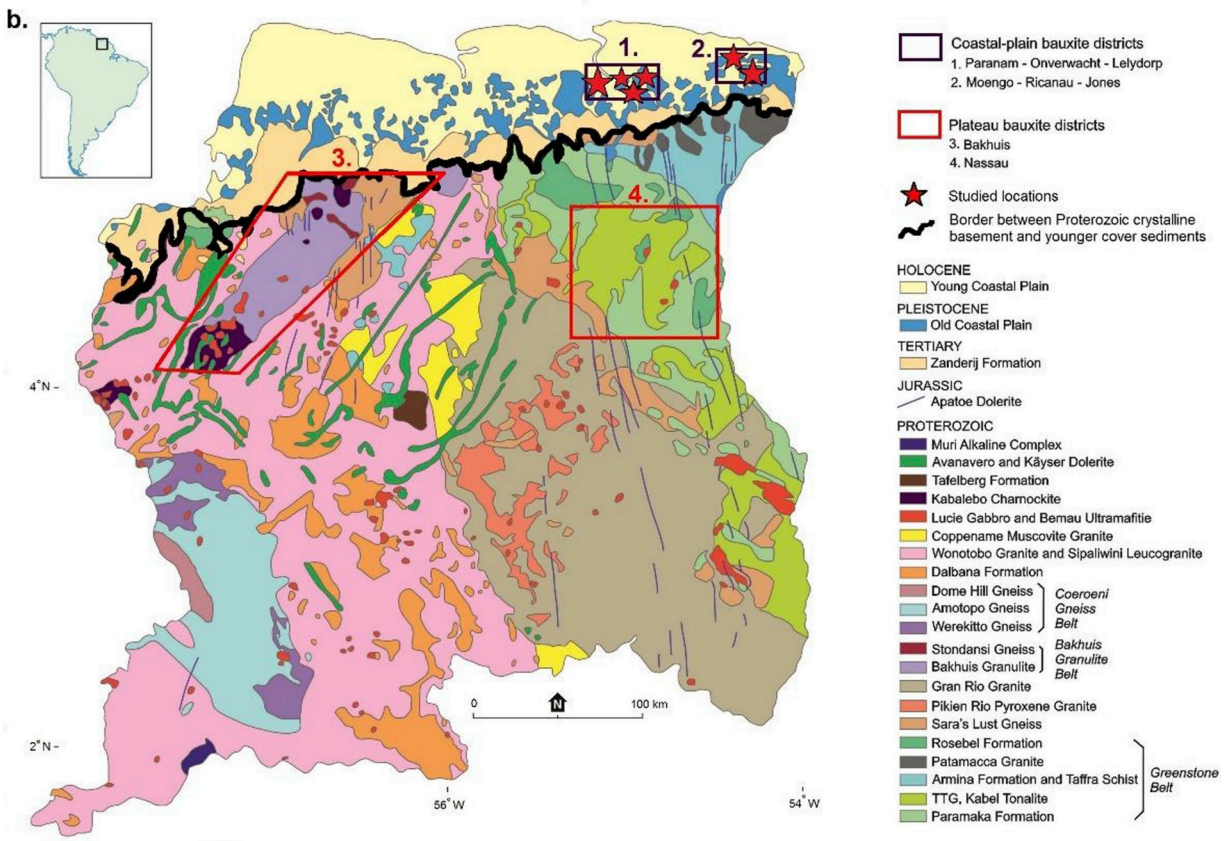


(caption on next page)

**Fig. 1.** (a) Geological sketch of the Guiana Shield and planation surfaces (modified after Théveniaut and Freyssinet, 2002). See Fig. 1c for their stratigraphic positions. Labelled arrows point to the study areas: POL = Paranam-Onverdacht Lelydorp district and MRJ = Moengo-Ricanau-Jones district; (b) Geological map of Suriname (modified after Kroonenberg et al., 2016) with bauxite districts and study locations. Areas 1 and 2 represent districts of coastal-plain bauxite deposits studied here, while areas 3 and 4 are districts of plateau bauxites developed on Proterozoic basement (see Monsels and Van Bergen, 2017). Fig. 1. (c) The planation levels, stratigraphy and pollen zones of Suriname (Van der Hammen and Wijmstra, 1964; Wong, 1989: Bárdossy and Aleva, 1990; Wong et al., 2009). The coastal-plain bauxites formed at the top of the exposed Onverdacht Formation during the "Bauxite hiatus" (period of non-deposition).

Guyana (Valeton, 1983; Aleva and Wong, 1998) (Fig. 1b). Similar to the world-class Paragominas, Trombetas, Juruti and Rondon do Pará deposits that developed on Cretaceous and Tertiary sediments in the Lower Amazon Basin south of the Guiana Shield (Grubb, 1979; Aleva, 1981; Lima da Costa et al., 2014; Oliveira et al., 2016), Suriname's lowland hosted some of the highest $Al_2O_3$-grade bauxites ores (frequently > 50%) worldwide.

There is ongoing debate on the nature of the precursor material, for which arkosic sandstone interlayed with clayey sediments (Aleva, 1965; Aleva et al., 1969; Krook, 1969b, 1979; Wong et al., 1998, 2009 and references therein) and kaolinitic clays (Bakker et al., 1953; Van Kersen, 1956; Moses and Michell, 1963; Doeve and Groeneveld Meijer, 1963) have been proposed. In addition to field relationships, trace-element signatures, in combination with petrographic and mineralogical constraints, can be helpful to solve this question, and are instrumental in exploring processes and controls of chemical weathering that accompanied bauxite formation, as well as in tracing the nature and provenance of precursor materials (Dennen and Norton, 1977; Abedini et al., 2014; Costa et al., 2014; Wei et al., 2014; Oliveira et al., 2016; Ahmadnejad et al., 2017; Ling et al., 2018). This study of lateritic coastal-plain bauxites of Suriname concentrates on these issues, documents their geochemical characteristics in the context of local geological settings, and discusses implications for their origin.

## 2. Geological background

The Proterozoic basement of Suriname occupies approximately 80% of the country and consists of igneous, metamorphic, and metasedimentary rocks, while the overlying unconsolidated sediments form the coastal plain (Fig. 1b). This coastal area is subdivided into two geomorphological units: the Young Coastal Plain in the North and the Old Coastal Plain in the south (Wong et al., 2009). The top section of the Paleocene-Eocene Onverdacht Formation, consisting of coarse clastic alluvial sediments, was converted into bauxite during the Late Eocene to Oligocene, which is characterized by a period of non-deposition also known as the *Bauxite Hiatus*. (Fig. 1c) (Wong et al., 2009). The Onverdacht Formation is found along a 10 km wide belt, approximately 40 km inland and stretching from ca. 40 km west of the Suriname River into French Guiana, which exclusively crops out in the Moengo area (Wong et al., 2009). The Onverdacht Formation is a time equivalent of the deltaic Saramacca Formation and the marine Alliance Formation (Fig. 1c) (Leonard, 1984; Wong et al., 2009). Kaolinitic clays and clayey sands of the Onverdacht Formation gradually change into alternating sands and kaolinitic clays of the Saramacca Formation northwards, which in turn passes into the Alliance Formation that consists of silty marls with intercalations of clays, sands and lignites (Wong, 1989; Wong et al., 2009).

### 2.1. Local geology of coastal-plain bauxite deposits

The Surinamese coastal-plain bauxite deposits are grouped into two districts (Fig. 1a and b):

(1) the Paranam-Onverdacht-Lelydorp (POL) district, and (2) the Moengo-Ricanau-Jones (MRJ) district.

#### 2.1.1. Paranam-Onverdacht-Lelydorp (POL) bauxite district

This bauxite district (Fig. 2) originally consisted of twenty deposits (Bárdossy and Aleva, 1990), the majority of which has been mined out in open pits (Monsels, 2016). The bauxite produced from these deposits was a high-grade trihydrate (gibbsite) type containing very little boehmite and silica (Patterson et al., 1986). A special group of bauxite deposits between the Suriname and the Commewijne rivers is known as the Successor Mines or Successor deposits, which include Klaverblad (KLB), Kaaimangrasie (KMG) and Caramacca (CRM). The KLB deposit is located along the east bank of the Suriname River, approximately 8 km downstream from the former refinery of Paranam, and the KMG and CRM deposits at 24 and 30 km east of it, respectively. These three deposits were only considered for mining after the high-quality and easy accessible POL deposits west of the Suriname River were exhausted (Fig. 2). The Klaverblad deposit had a initial reserve of 6000 Mt, Caramacca contained 5600 Mt, while Kaaimangrasie was the smallest deposit with a tonnage of 2700 Mt (BHP feasibility study, 2004). Some of the POL deposits had outcrops (Rac-A-Rac, Rorac, Accaribo and Topibo-de Vrijheid), whereas the majority was covered by a thick (up to 16 m) packet of Neogene-Quaternary sediments (Bárdossy and Aleva, 1990; cf., Wong et al., 2009). The overburden at KLB was on average ca. 15 m thick and consisted of Miocene-Holocene sediments, while the KMG and CRM deposits were covered by Pleistocene-Holocene sediments with average thicknesses of 3 and 9 m, respectively. Most of the POL deposits were also covered by swamps which required a special mining method of wet dredging of the upper clays followed by bucket-wheel stripping of the remaining lower overburden. Most of the bauxite-capped hills of this bauxite district are underlain by Early-Eocene and Paleocene sediments (Fig. 1c). Precambrian basement was encountered 25 m below the KLB deposit (−40 m MSL) (BHP feasibility study, 2004). Contour maps of the Successor deposits revealed that the bauxite horizon usually capped 10–40 m high dome-shaped residual hills above the Late Cretaceous planation surface, which now slopes 1–2° N (Fig. 3b). The deposits generally have the shape of a concave lens, with the largest thickness (up to 12 m) in the centre and thinner (< 1.0 m) lower-lying edges. In this extended POL district, the Successor deposits (KLB, KMG and CRM), Lelydorp-1, Kankantrie (Noord) and Para (Noord) deposits were studied here.

#### 2.1.2. Moengo-Ricanau-Jones (MRJ) bauxite district

This bauxite district, also known as the "Moengo Group of deposits", is located in the eastern part of the Suriname coastal plain (Fig. 1a and b, 4 and 5). This bauxite-capped plateau is the only known outcrop of the Onverdacht Formation, as the Pleistocene transgression did not reach much further south than the foot of these hills near the village of Moengo (Bárdossy and Aleva, 1990). The plateau initially had a total surface area of approximately 20 $km^2$, split over 25 hills with sizes between 0.03 and 7 $km^2$, and with elevations decreasing from +75 m in the south to −40 m in the north (Bárdossy and Aleva, 1990) (Figs. 4 and 5). In a N-S cross section the bauxite deposits of this district show an overall northward dip (Fig. 5). The bauxite-capped hills are erosion remnants of one or more relatively large peneplains incised by a drainage pattern (Aleva, 1979, 1984; Wong, 1989; Bárdossy and Aleva, 1990). Using a palaeomagnetic approach, Théveniaut and Freyssinet (2002) found a much younger age of 10 Ma for the Moengo coastal bauxite than the generally accepted Eocene age of the Surinamese coastal plain deposits (Aleva, 1965; Wijmstra and Van der Hammen, 1964; Pollack, 1983; Bárdossy and Aleva, 1990). This young palaeomagnetic age is possibly due to polycyclic bauxitization and resetting of the initial age, which may have been promoted by the absence of a significant overburden on this deposit (Monsels and Van Bergen, 2017).

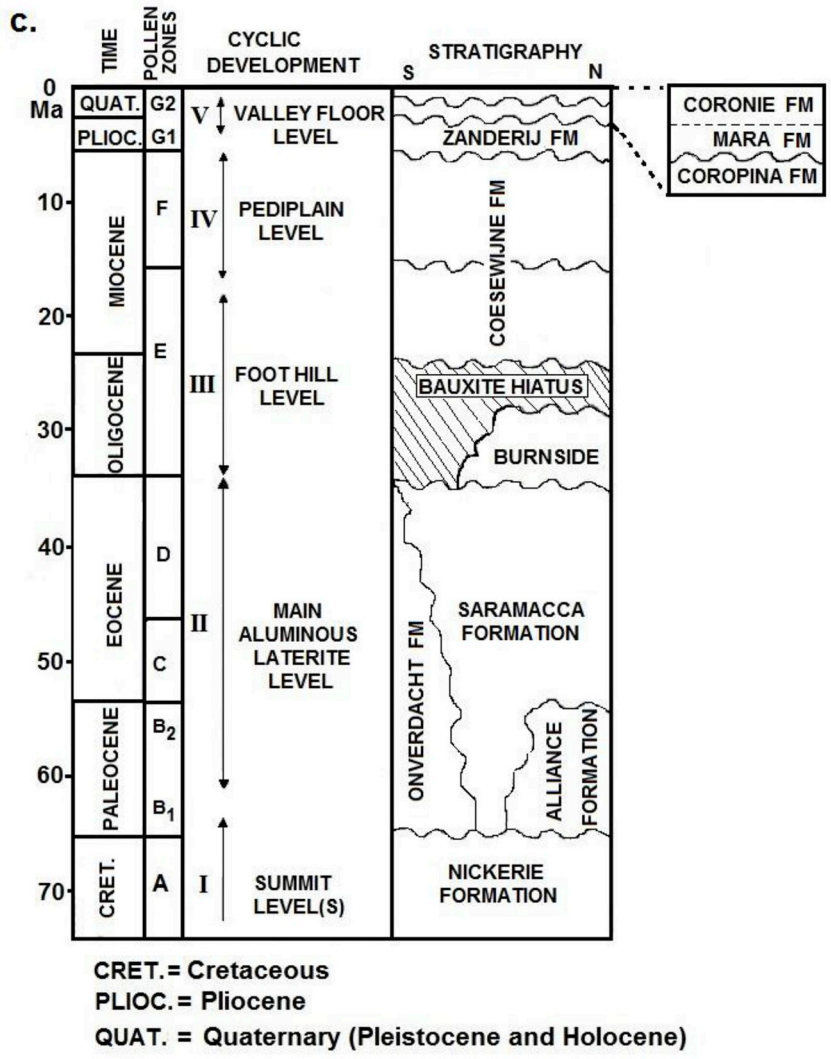


**Fig. 1.** (*continued*)

The bauxite layer of the mined deposits was generally 3–6 m thick, and the original geological reserve approximately 127 Mt (Bárdossy and Aleva, 1990). The bauxite deposits in this district are also mined out, with the exception of the Coermotibo deposit (CBO) studied here.

This deposit, named after the nearby Coermotibo River, has a reserve/resource of 18/37 Mt and is the only buried MRJ deposit, being covered by a ca. 40 m thick overburden (Bárdossy and Aleva, 1990) (Figs. 4 and 5). Despite its high aluminium grade (average 51 wt% $Al_2O_3$) and low iron content (average 4 wt% $Fe_2O_3$) (Bárdossy and Aleva, 1990) the Coermotibo deposit has not been exploited to date, because of a resilication imprint, its 40 m thick overburden, its generally clayey bauxite texture, and a high sulfur content (average 7.1 wt %, maximum 60 wt% $SO_3$), linked to large quantities of marcasite (Janssen, 1970, 1979; Monsels, 2016).

## 3. Materials and methods

### 3.1. Sample locations and studied materials

The studied sites on which we report here are the Successor deposits (KLB, CRM, KMG), Lelydorp-1, Para (Noord) and Kankantrie (Noord) in the POL bauxite district (Fig. 2), and Coermotibo and the East Group of Hills (Adjoema, Madoekas and Lobato Hills) in the MRJ bauxite district. Sampling of the Successor and Lelydorp-1 deposits was performed when the mines were still in operation.

Samples from the lateritic weathering profiles of Klaverblad (n = 13), Kaaimangrasie (n = 10) and Caramacca (n = 11) were collected down to a depth of 7.0, 5.0 and 6.75 m, respectively, at variable vertical intervals of 25, 50 or 100 cm, depending on lithofacies changes. Supplementary samples of KLB (n = 4), CRM (n = 1) and KMG (n = 1) were collected for comparison and reference purposes. In all of these cases, “chip and grab samples” were taken from fresh mine faces with a hammer or scoop, depending on the consistency of the material. The weathering profiles of Coermotibo are based on drillcore samples (Monsels, 2004). Externally provided compositional data for Lelydorp-1, Kankantrie (Noord), Para (Noord) and Coermotibo, as well as data for the East Group of Hills from Diko et al. (2001) are all based on drill cuttings. It should be noted that not all of the POL and MRJ profiles reached the underlying kaolinitic clays, as the mining companies stopped drilling and excavating after reaching this level. Soil color descriptions are based on the Munsell color charts.

### 3.2. Analytical methods

Microscopic and geochemical analyses of samples from the Successor deposits were performed at Utrecht University and VU University Amsterdam. Mineralogy and microtextures were investigated on polished thin sections with an optical microscope and an electron microprobe (JEOL JXA-8600 Superprobe) using both energy dispersive (EDS) and wavelength-dispersive (WDS) analytical

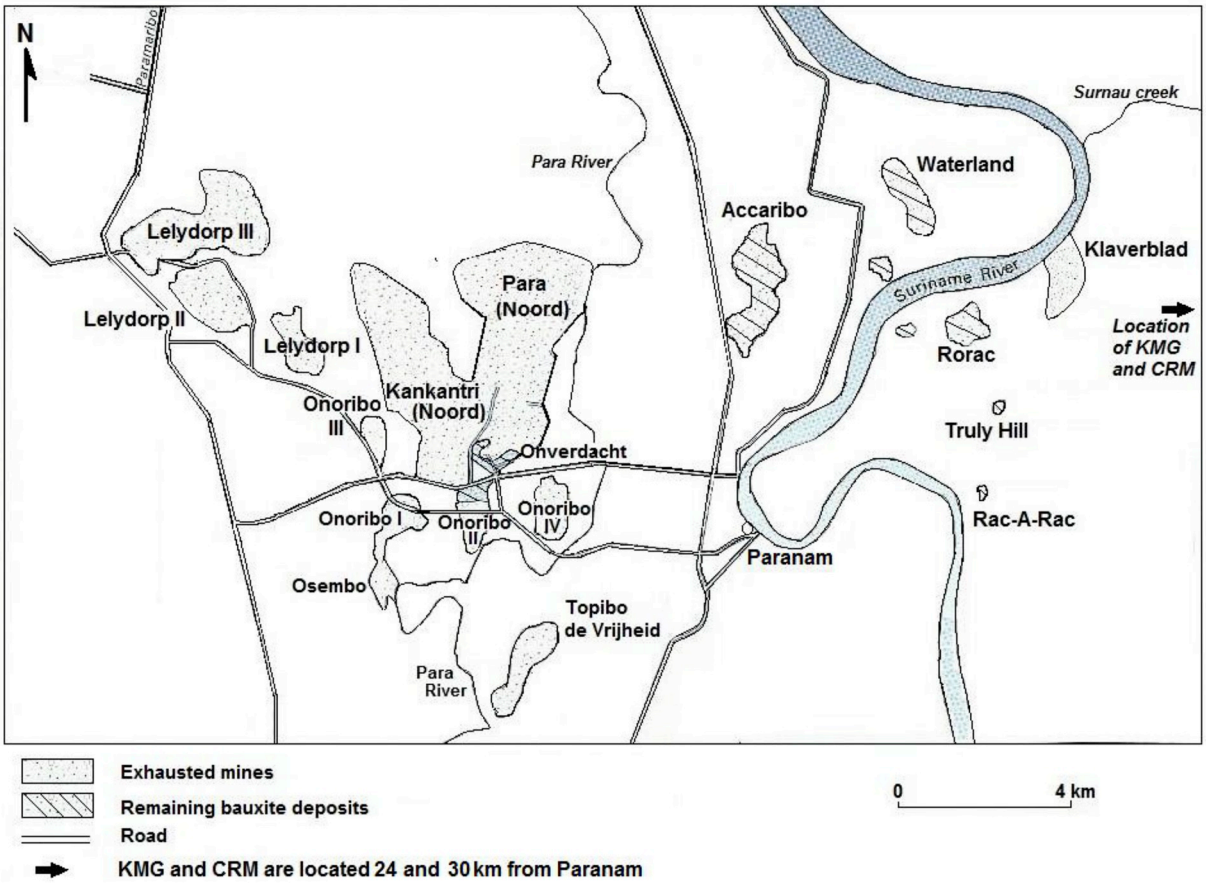


**Fig. 2.** Map of the original bauxite deposits of the Paranam-Onverdacht-Lelydorp (POL) bauxite district. KMG and CRM are not depicted on this map, but are located 24 and 30 km east of Paranam (see Fig. 3a). The current surface area is significantly reduced since most of the deposits have been mined out. Study areas comprise the three Successor deposits and the Lelydorp-1, Kankantrie (Noord) and Para (Noord) deposits (modified after SPS & OAS, 1988).

techniques. Back-scatter electron imaging (BSE) was used to identify mineral phases and to study textural relationships. Quantitative compositions of mineral phases were determined via EDS microprobe analysis in representative domains of selected samples. X-ray diffraction (XRD) patterns were collected from randomly oriented powder samples using a Bruker D2 Phaser X-ray diffractometer, operated in a step-scan mode, with Co-Kα radiation (1.78897 Å). The counting time was 66 s/step, the step size $0.05^0$ and the range $5\text{-}85^0$. Total acquisition time per sample was approximately 15 min. Major-element compositions of the Successor samples were determined by X-ray fluorescence (XRF) on fused glass beads (lithium borate) with a Thermo ARL 9400 sequential XRF (Utrecht University) and a Panalytical MagiXPro XRF (VU University Amsterdam). Loss-on-ignition data were obtained either by measuring weight loss upon heating of a powdered sample in an oven at > 1000 °C or by thermogravimetric analysis (TGA) during which weight loss was continuously monitored over a temperature range between room temperature and 1000 °C. Major-element XRF data for Lelydorp-1 and Coermotibo were provided by Suralco L.L.C., those for Kankantrie (Noord) and Para (Noord) by the Bauxite Institute Suriname, and those for the East Group of Hills are from Diko et al. (2001).

Trace-element concentrations in the Successor samples were determined by laser ablation-inductively coupled plasma-mass spectrometry (LA-ICP-MS) on the fused glass beads prepared for XRF, using a ThermoFischer Scientific Element 2 magnetic sector instrument, integrated with a Lambda Physik excimer laser (193 nm) with GeoLas optics. Details of the procedure are outlined in Monsels et al. (2018). Main parameters for the ablation spot setup were: 5 mJ laser energy, 10 Hz pulse repetition rate and 120 μm spot diameter. The ICP-MS operating conditions were plasma power: 1300 W; gas flow rates (L/min): cool 16.0 Ar, auxiliary 1.0 Ar, carrier: 0.685 He, 0.696 He; peak-jump scanning mode; time-resolved acquisition mode; 60 s total ablation time. Si was employed as internal standard. SRM-NIST 612 was used during the measurements to correct for background and drift with double-standard measurements bracketing each six samples. Reported compositions are averages of three measurements for each sample. Accuracy of the results was monitored by analyzing USGS standard BCR-2 after each six samples. The percentage of deviation from recommended values, determined in multiple sessions, was generally ≤10% for all reported trace elements (Monsels et al., 2018).

## 4. Results and discussion

### 4.1. Field appearances, textures and mineralogy

#### 4.1.1. Successor deposits (Klaverblad, Kaaimangrasie and Caramacca)

The bauxite-bearing deposits of this group are marked by a strong lateral and vertical heterogeneity on a macroscopic and microscopic scale. They typically consist of three main horizons: kaolinite-rich saprolitic clays at the bottom (from hereon referred to as “kaolin” in view of an unclear relation with the underlying sediment), an intermediate gibbsite (Al)-rich bauxite zone in various forms of appearance, and an iron-rich zone with abundant hematite or “duricrust” at the top (Fig. 6 a,b and 7a,b). A complete section of the KLB deposit hosting a homogeneous high-quality bauxite with an average $Al_2O_3$ content of 57 wt% is depicted in Fig. 6a (BHP feasibility study, 2004). The sampled location in the last remaining section of the KLB mine (Fig. 7b) was heterogeneous and hosted a lower-quality ore (average $Al_2O_3$ content of

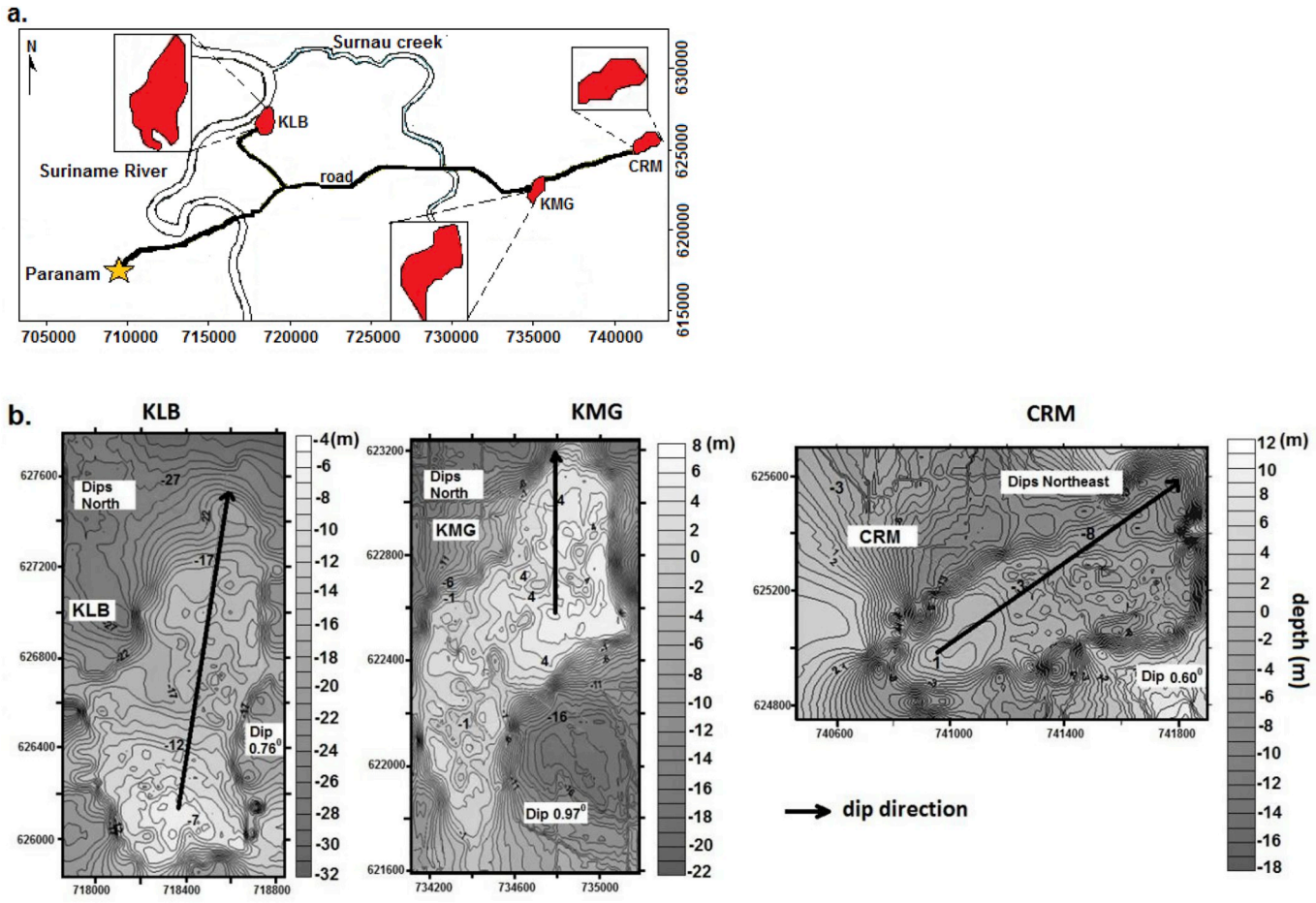


**Fig. 3.** (a) Location of the Succesor deposits: Klaverblad (KLB), Kaaimangrasie (KMG) and Caramacca(CRM); (b) Contour maps of the top of the bauxite ore at the Successor deposits, showing that the deposits are located on buried hills, each dipping in a different direction (modified after Kisoensingh, 2009).

49 wt%). The iron-rich duricrust had already been removed by the mining company before sampling commenced. For these reasons, the following description largely concentrates on the bauxite interval (see Table 1).

The bauxite horizon in the three Successor deposits was generally 4–6 m thick. Its multicolored matrix, mottles and lenses range from white (2.5 YR 8/2), light yellow/crème (10 YR 8/1–8/6) to red (2.5 YR 5/8), dark brownish red (2.5 YR 8/3) and reddish black (2.5 YR 2.5/1) (Fig. 8a–e). Macroscopic textures and other properties of the Successor bauxites are summarized in Table 2.

The bauxite horizons are marked by strong lateral variations, generally showing abrupt transitions in color and/or texture (Fig. 6b1,b2 and 8a,b). Color changes are primarily linked to iron content, with red and yellow bauxites being rich in hematite and goethite, respectively, and white bauxite only containing a few percent of iron.

Paleochannels observed in the duricrust of all three Successor deposits provide field evidence for reworking as is illustrated by paleochannel infill of a dark brownish-red mixture of breccia-like and massive bauxite in the KLB profile (Fig. 6b1 and b2). The Successor deposits share these features with other coastal-plain bauxites (POL and MRJ deposits), fitting in a landscape evolution (Bárdossy and Aleva, 1990) wherein narrow winding valleys, developed during marine regressions or coastal uplifts, were later filled with sediments and/or eroded bauxite during Miocene and Pliocene-Pleistocene transgressions, which eventually covered the flat-topped bauxite hills as well. This scenario is consistent with a two-step origin of the bauxite involving (1) mechanical erosion and alluvial transport of an earlier lateritic bauxite formed at a higher elevation, and (2) re-bauxitization of the accumulated alluvial bauxite, as has been proposed for the Surinamese coastal plain bauxites (Bleackley, 1964; Moses and Michell, 1963; Krook, 1969), as well as for the Sangaredi district in West Africa (Gow and Lozej, 1993; Chardon, 2006).

*4.1.1.1. Textures.* Various tubular-shaped textures such as root-shaped concretions, were observed in basal parts of the Successor bauxite deposits (Fig. 8j, l), and fossilized empty or filled tubulesand burrows in upper parts of the investigated sections (Fig. 8l). Similar root-shaped concretions and tubules have also been reported in bauxite from other POL deposits (Lelydorp-1, Kankantrie, Onoribo-1, Topibo de Vrijheid), MRJ deposits (Ricanau, Coermotibo), Linden-Berbice district in Guyana and the Paragominas bauxite district in Brazil (Valeton, 1971, 1983; Bárdossy and Aleva, 1990; Carvalho et al., 1997). These concretions have also been observed in clay and sandstone layers below the bauxite at Onoribo-1, Topibo de Vrijheid and Ricanau (Valeton, 1971, 1983). No data on underlying strata are available for the Succesor Mines. The root- and rod-shaped concretions blend in with the color of the host matrix, which points to their *in situ* formation as authochthonous relic textures (Fig. 8l). The bioturbation and root horizons formed in the original sedimentary parent material or soft bauxite under synsedimentary to early diagenetic conditions, given the ease for vegetation and invertebrates to penetrate soft soil compared to hard massive duricrust and bauxite. Microscopic analysis of these burrows and concretions either revealed an internal “Fill-in”/“Stopfgefüge” texture (Valeton, 1971) or a complete lack of structure (Fig. 8k and f). The “Stopfgefüge” texture can be described as distinctive, flatly concave layering, usually perpendicular to the length direction of the tube. It formed as a result of mechanical illuviation where percolating meteoric water reached a drier soil horizon, and water from the

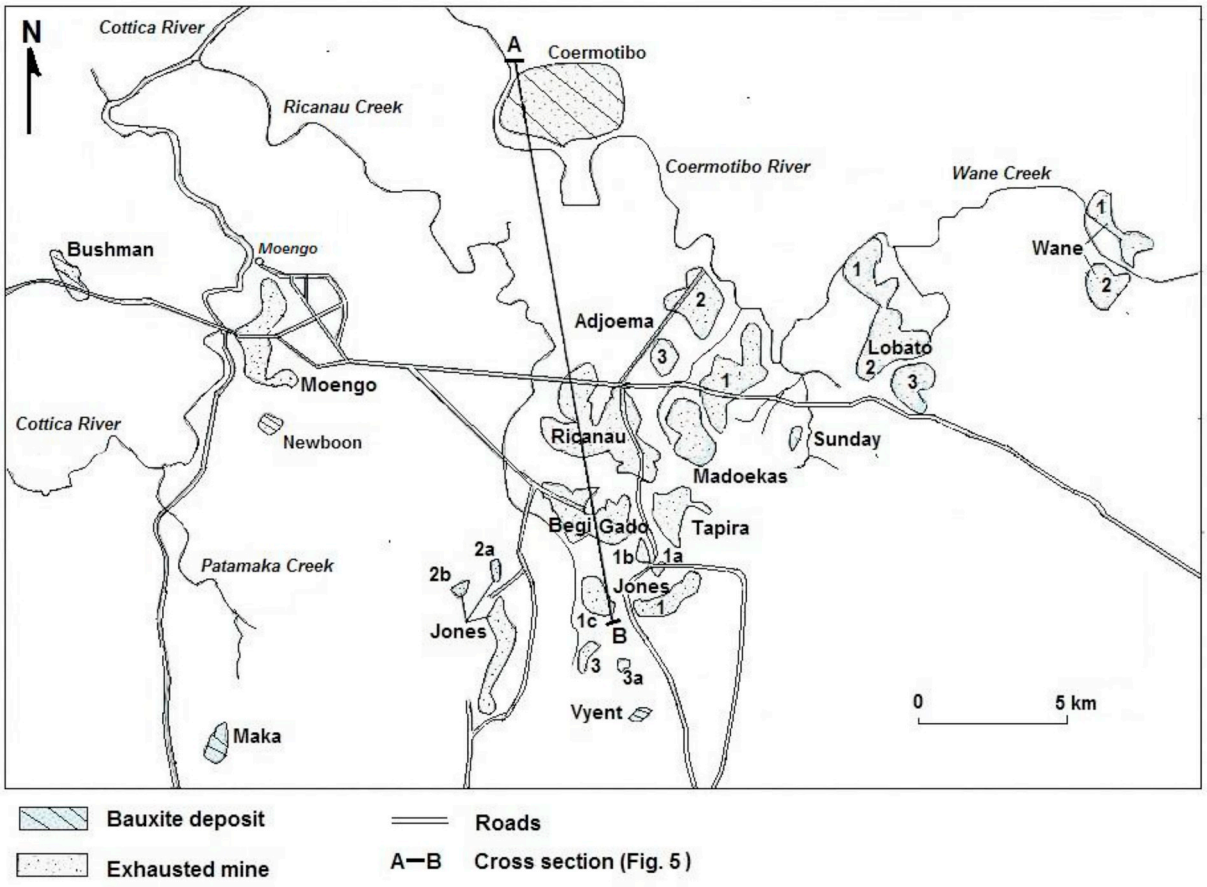


**Fig. 4.** Original distribution of the depositsin the Moengo-Ricanau-Jones district (modified after SPS & OAS, 1988).

suspension was removed by absorption, evaporation or capillary action, leaving fine deposits (cutans) oriented along percolation macrochannels (Velde and Meunier, 2008). The filling material is predominantly cryptocrystalline or coarse-grained gibbsite with traces of kaolinite and/or hydrated iron oxides (Fig. 8f, l).

In the earthy bauxite of the KLB deposit, several grey (2.5 YR 7/1) silica-rich lenses were encountered, which contained quartz grains, pink Al-rich concretions and traces of organic matter (Figs. 7b, 8e and 9c). These lenses and concretions usually had a goethite-rich coating. The quartz grains were detected both in petrographic thin sections and in XRD analysis (Fig. 10b).

*4.1.1.2. Mineralogy*. The analytical investigations of the Successor bauxite samples detected the presence of gibbsite, hematite, goethite, anatase and other Ti-oxides, as well as minor quantities of quartz and zircon, in line with observations elsewhere in the coastal-plain deposits (e.g., Van der Hammen, 1969; Bárdossy and Aleva, 1990).

Hematite is finely dispersed in the bauxite as stains, mottles (glaebules), nodules and concretions, whereas it formed euhedral to subhedral crystals in voids (Fig. 8a–e). Goethite mainly formed coats around grey silica-rich lenses and gibbsite- and hematite-rich nodules. The cryptocrystalline gibbsite or hematite-rich nodules and concretions are generally embedded in a earthy to clay-like bauxite matrix. They occasionally have a hematite, goethite or gibbsite coating. The prominent mottles vary in size, shape (irregular or oval) and color, from white (10 YR 8/1), crème (10 YR 8/3), red (2.5 YR 5/8) yellow (2.5 YR 7/8) to reddish black (10R 2.5/1). They sometimes appear to be tubular or vermicular in cross-section (Fig. 8d).

The texture of the gibbsitic bauxite matrix varies from aphanitic (clay-size) to coarse-grained, while voids, veins and burrows are lined

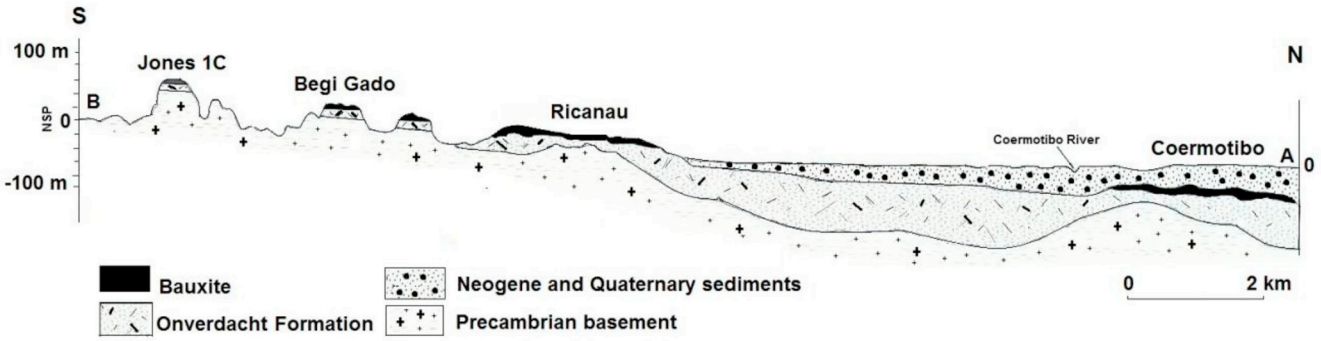


**Fig. 5.** South-North section through the Moengo-Ricanau-Jones district showing the northward dip of the bauxite layer and the buried position of the Coermotibo deposit (Fig. 4) (modified after SPS & OAS, 1988).

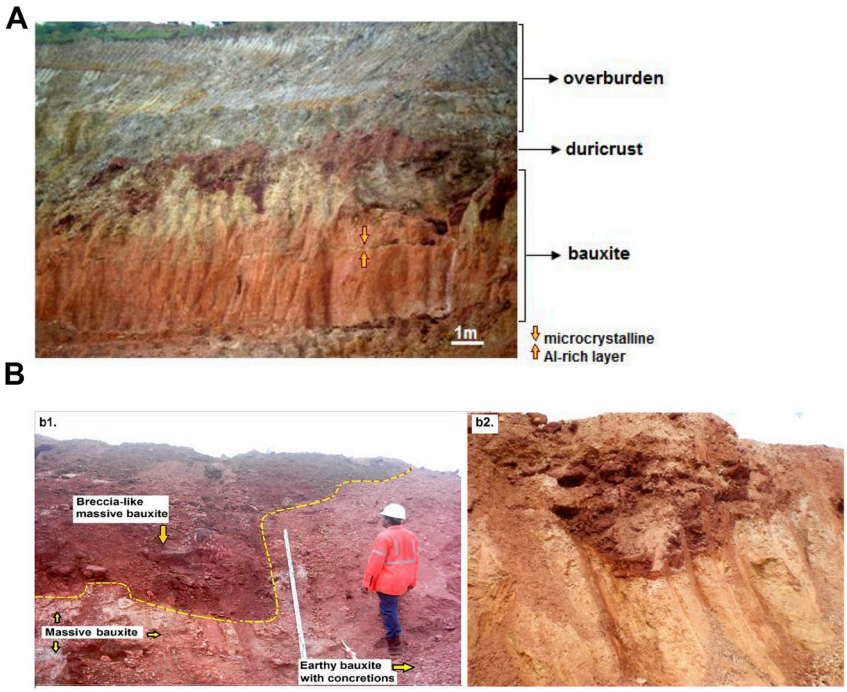


**Fig. 6.** a. Weathering profile of the Klaverblad (KLB) deposit with overburden (not the sampling location). Note the hard microcrystalline Al-rich layer in the bauxite horizon. Fig. 6b. (b1) Sampling location of weathering profile in the KLB deposit. Note the heterogeneous, irregular distribution of lithofacies, textures and colors. Dotted line depicts the sharp irregular boundary between the facies. The dark red iron-rich part resembles a paleochannel infill similar to that in b2; (b2) Funnel-shaped iron-rich duricrust within light-colored bauxite at KLB. (For interpretation of the references to color in this figure legend, the reader is referred to the Web version of this article.)

or filled with coarse-grained secondary gibbsite crystals (Fig. 8f–h). The BSE image of Fig. 8f shows three texturally different gibbsite-bearing domains: (1) a dark-grey aphanitic gibbsite-rich matrix, (2) medium-grey fine-grained dispersed gibbsite crystals and (3) a light-grey coarse-grained crystals. The color differences mainly reflect relative abundances in Fe or Ti as staining or substitutions. These morphological textures (cf., Delvigne, 1998) point to at least two different generations of gibbsite. The first consists of a fine-to coarse-grained gibbsite-rich matrix (crypto-alteromorphs) after kaolinite (Fig. 8f) produced by the desilication reaction:

$$Al_2Si_2O_5(OH)_4 + H_2O \rightarrow 2A1(OH)_3 + 2SiO_2\ (aq)$$

This reaction is a function of silica and water activity, humidity, depth to the water table, and the presence of other ions (Carvalho et al., 1997; Tardy, 1997; Zhu et al., 2006, 2010; Wei et al., 2014). There are no indications for direct conversion of feldspar into gibbsite, as observed in the Plateau bauxites of Suriname (Monsels and Van Bergen, 2017). The second generation of gibbsite appears as coarse-grained void linings (Fig. 8g and h), which originated from the precipitation and aging of colloidal Al-rich solutions migrating through the bauxite horizon and in the transition zone near the root-shaped concretions. Multiple gibbsite linings in voids and perpendicular orientation of grains against the walls of voids, pores and burrows are consistent with in-situ precipitation of an allochthonous illuvial Al-gel. Spiral growth of the tabular gibbsite crystals (Fig. 8g), also reported from bauxites in India (Valeton, 1972), reflects the degree of supersaturation (Lee and Parkinson, 1999). A white, up to a 8 cm thick layer, rich in microcrystalline gibbsite, locally occurs over several meters in the KLB deposit (Figs. 6a and 8i), and presumably precipitated from an Al-rich solution upon a fluctuation of the groundwater level.

Kaolinite is the dominant silica-bearing phase in the transition zone and kaolin of the Successor Mines. These zones have variable heavy mineral contents and display sedimentary features such as layering or bedding planes inherited from the sedimentary precursor. The kaolinite was observed in the form of flakes and vermicular stacks. The kaolin horizon also contained variable amounts of mica, quartz and hematite (Figs. 9f and 10c-d). XRD patterns of CRM kaolin samples revealed the presence of hematite, responsible for its purple color, while white KLB and KMG kaolin samples were both iron deficient (Fig. 10a and b).

The *Ti-phases* such as anatase, rutile and ilmenite frequently form clusters or accumulate near a boundary, for example between gibbsite-rich and kaolinite-rich domains in the bauxite matrix (Fig. 9d). Weathering of anatase and other Ti-phases created complex intergrowths of secondary Ti-rich phases (Fig. 9a) or peculiar boxwork textures (Fig. 9e and g). These secondary Ti-oxide phases were only identified by electron microprobe analysis, whereas XRD-analysis only detected anatase, presumably because overlapping peaks of more abundant kaolinite and other major phases may have obscured the minor phases (Fig. 9a,d and 10a). This presence of multiple Ti-oxides in the Successor deposits points to formation as alteration product of primary oxides (cf., Grey and Reid, 1975; Anand and Gilkes, 1984; Cornu et al., 1999) or inheritance from the sediment source.

The quantity of (sub-)euhedral to sub-rounded *heavy minerals* such as zircon, ilmenite, anatase, rutile and tourmaline increases towards the bottom of the Successor lateritic profiles. They usually accumulate and display a vague sedimentary layering in the transition zone and the kaolin (Fig. 9a and b, 10). Zircon grains in the three Successor deposits can be small and rounded or subhedral to euhedral (Fig. 9a and b). The latter show signs of zonation and re-growth textures, suggesting complex crystallization histories reminiscent to reported textures of zircons in the Coermotibo deposit, which have been attributed to authigenic growth (Van der Laan, 1998). This textural diversity could be due to sediment provenance, either from different sources or from a single source with a heterogeneous zircon population.

#### 4.1.2. Lelydorp-1 deposit

The schematic representation of lithofacies of the Lelydorp-1 deposit (Fig. 11a1) shows a roughly similar subdivision into three main horizons (duricrust-bauxite-“kaolin”) as the Successor deposits, albeit with differences in detail. The main bauxite layer in this deposit ranged in thickness between 0.5 m and 12 m. Noticeable features are:

1. Iron- and clay-rich pockets in the bauxite (Fig. 11a1, 11b)
2. Bauxite dikes in the underlying saprolite (Fig. 11c)
3. Kaolinite-rich diapir-like structures which penetrate the bauxite horizon from below. These were presumably formed during the Oligocene, when the bauxite-capped hills dried out down to considerable depth. The resulting fissures enhanced the permeability of

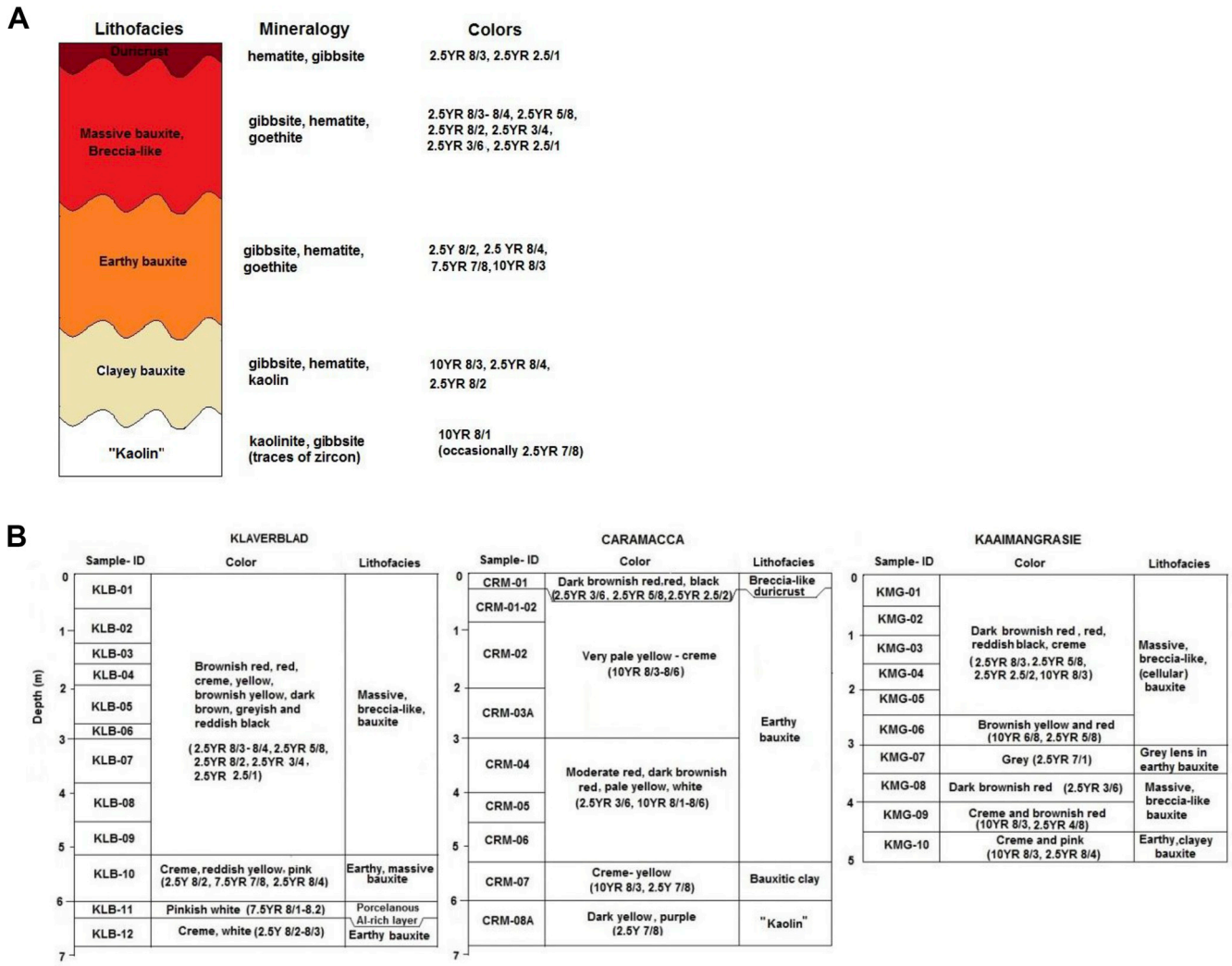


**Fig. 7.** a. Generalized weathering profile of the Successor Mines (KLB, KMG, and CRM). "Kaolin" is the underlying kaolinite-rich clay layer (see text). Color codes according to the Munsell color system. Fig. 7b. Sampled lateritic profiles of the Successor Mines (KLB, KMG and CRM). Color codes according to the Munsell color system. (For interpretation of the references to color in this figure legend, the reader is referred to the Web version of this article.)

the initially impervious sediments and led to resilication of these fractures (Bárdossy and Aleva, 1990).

4. A secondary bauxite layer in the underlying saprolitic clays (Kaolin).
5. Depending on the location within the deposit, the underlying kaolinite-rich saprolitic clays had different appearances, ranging from pure white (iron-poor) to a layered texture with purple, more iron-rich beds (Fig. 11e and g). The kaolin also contained clusters of coarse-grained colorless micas in certain areas, as also observed in the Successor Mines and MRJ deposits (Figs. 9f, 11e and 13 f-g, 11e). The micas are a strong indication for the nearby presence of weathered basement. This basement was reported at the southern margin of the Onoribo II deposit, where saprolite of Precambrian gneisses, schists, granites and pegmatitic veins is directly overlain by bauxite. An extremely weathered basement (up to 10 m thick saprolite) was also encountered in drill holes in the coastal area, where it was occasionally only recognizable as bedrock because of the abundance of mica (Aleva et al., 1969; Van der Hammen, 1969; Bárdossy and Aleva, 1990). The variable properties of underlying sediments and kaolin provide evidence that the clays below the bauxite may not be the pre-weathering precursor (Bárdossy and Aleva, 1990; Valeton, 1972).
6. Spheroids in the transition zone varying between 1 and 30 cm (Fig. 11d–f).

These spheroids or bulbous concretions have also been reported from the Onoribo I and Moengo deposits (Valeton, 1979). Their cores are either empty or filled with gibbsite or kaolinite, whereas their 1–4 cm thick walls revealed relic parallel layering of alternating crème (10 YR 8/3, gibbsite with traces of kaolinite) and pink bands (2.5 YR 8/4, gibbsite with traces of iron and kaolinite) (Fig. 11f). They were mainly found in the transitional zone between the bauxite and the underlying kaolinitic layer of the Lelydorp-1 deposit. Little is known about their formation but the absence of concentric shells, and horizontal layering in their thick walls point to a different origin than that of pisoids. Spheroidal shapes are generally formed where isotropic media control diffusion rates so that reactants (e.g., mobilized Al and Fe) diffuse outward from the concretion centre at a balanced rate (Tardy and Nahon, 1985; Taylor and Eggleton, 2008; Chan et al., 2012). Formation of the bauxite spheroids might be analogous to that of hollow iron concretions (Putthapiban et al., 2007; Chan et al., 2012), whereby sedimentary deposition of the host material is followed by a sequence of chemical reactions (such as Al and Fe mobilization and re-deposition) and the hard outher shell protects the structure against weathering and erosion. The spheriodal shapes had possibly already formed in the layered host rock (arcosic sandstone) before bauxitization took place. The gibbsite or kaolinite in the spheroid cores are probably a precipitation product of gel solutions that percolated through cracks and walls.

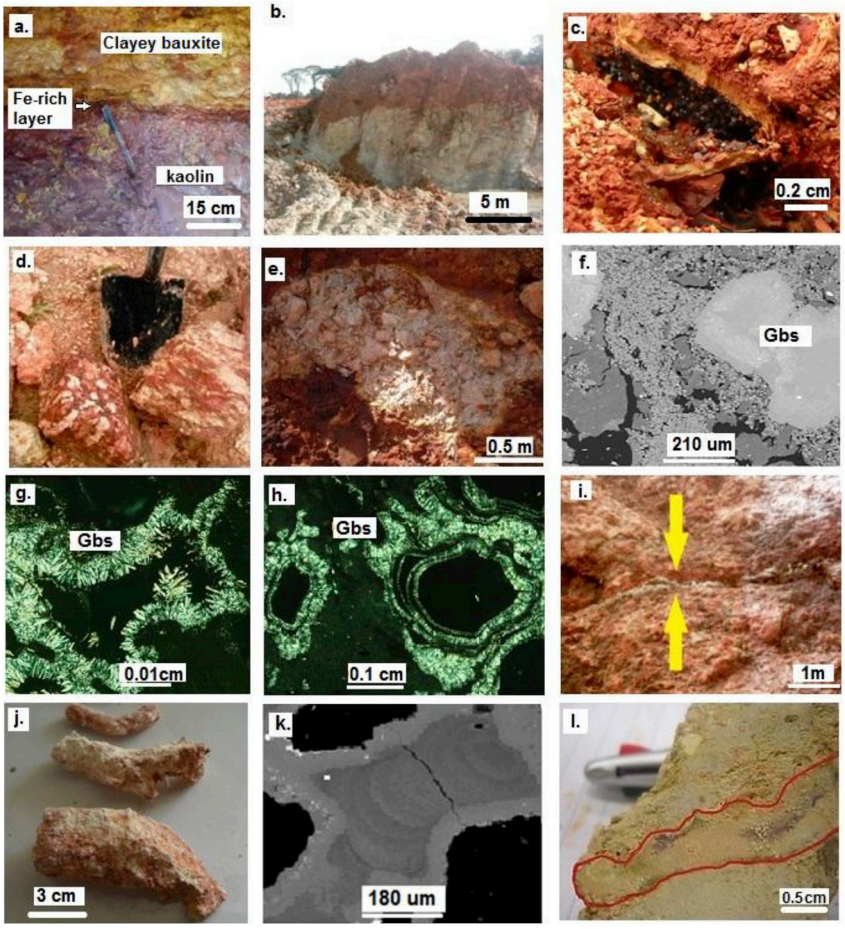


**Fig. 8.** (a) Sharp contact between clayey bauxite to purple colored kaolin (saprolite) with an iron-rich layer at the boundary in KMG; (b) Abrupt transition between red and white bauxite in CRM; (c) Euhedral to subhedral hematite crystals lining a void in the bauxite zone of CRM; (d) Side view of some mottled massive bauxite blocks in KMG; (e) Grey $SiO_2$-rich lens containing pink Al-rich concretions with a yellow goethite coating, surrounded by earthy bauxite in KMG; (f) BSE microphotograph of three different gibbsite textures in KMG-11. See text for explanation; (g) Microscope image of prismatic secondary gibbsite (Gbs) cluster, filling void in sample KLB-05 (XPL); (h) Microscope image of voids filled with multiple coarse-grained gibbsite (Gbs) linings in sample KLB-01 (XPL); (i) 4–8 cm thick white porcelanous Al-rich layer in massive bauxite from KLB; j) Root-shaped concretions of the KMG deposit; (k) BSE image of a burrow with "Stopfgefüge" illuviation texture in sample KLB-16; (l) Burrow (highlighted with red line) filled with crème cryptocrystalline Al-rich material in CRM. (For interpretation of the references to color in this figure legend, the reader is referred to the Web version of this article.)

**Table 1**
Overview of sample types, applied analytical methods and sources. BIS = Bauxite Institute Suriname.

| Study area | Samples | Analytical methods | Source |
|---|---|---|---|
| *POL District* | | | |
| Successor deposits (KLB, KMG, CRM) | Chip and grab samples | Macroscopic analysis, XRF, XRD, LA-ICPMS, optical microscope, electron microprobe analysis (Utrecht Univ.) | *This work* |
| Lelydorp-1 | Chip and grab samples | Macroscopic analysis | *This work* |
| | Cuttings from grade-control sampling | XRF (Suralco lab) | Suralco |
| Para (Noord) | Cuttings from exploration drill holes | XRF and FTIR (Suralco lab) | BIS |
| Kankantrie (Noord) | Cuttings from exploration drill cores | XRF and FTIR (Suralco lab) | BIS |
| *MRJ District* | | | |
| East Group of Hills | Cuttings from grade-control sampling | XRF and FTIR (Suralco lab) | Diko et al. (2001) |
| Coermotibo | Drill core samples from exploration drill holes | Macroscopic analysis | Monsels (2004) |
| | Cuttings from exploration drill holes | XRF and FTIR (Suralco lab) | BIS |
| Madoekas | Chip and grab samples from remants of the exhausted mine | Macroscopic analysis, XRF, XRD, optical microscope, electron microprobe analysis (Utrecht Univ.) | *This work* |

**Table 2**
Textures and other properties of the Successor Mines bauxites arranged from most dominant to least observed.

| Texture | Consistency | Other characteristics |
|---|---|---|
| Massive | Extremely hard | Generally at the top of the bauxite horizon; can also contain bauxite nodules |
| Breccia-like | Hard - Extremely hard | Contains relics of lateritic duricrust (high iron content) and pieces of massive bauxite |
| Clay-like | Soft | Has sticky, clayey feel; high $Al_2O_3$ content |
| Earthy (nodular) bauxite | Loose | Bauxite nodules bedded in a loose friable matrix; presence of $SiO_2$-rich, grey lenses |
| Cellular | Hard | Hard matrix with voids, occasionally lined with subhedral gibbsite or hematite crystals |
| Layered | Friable | Alternating red and crème-colored layers, usually present in the transition zone between the bauxite and "kaolin". Observed in the Caramacca and Lelydorp-1 deposit (Kisoensingh, 2009) |

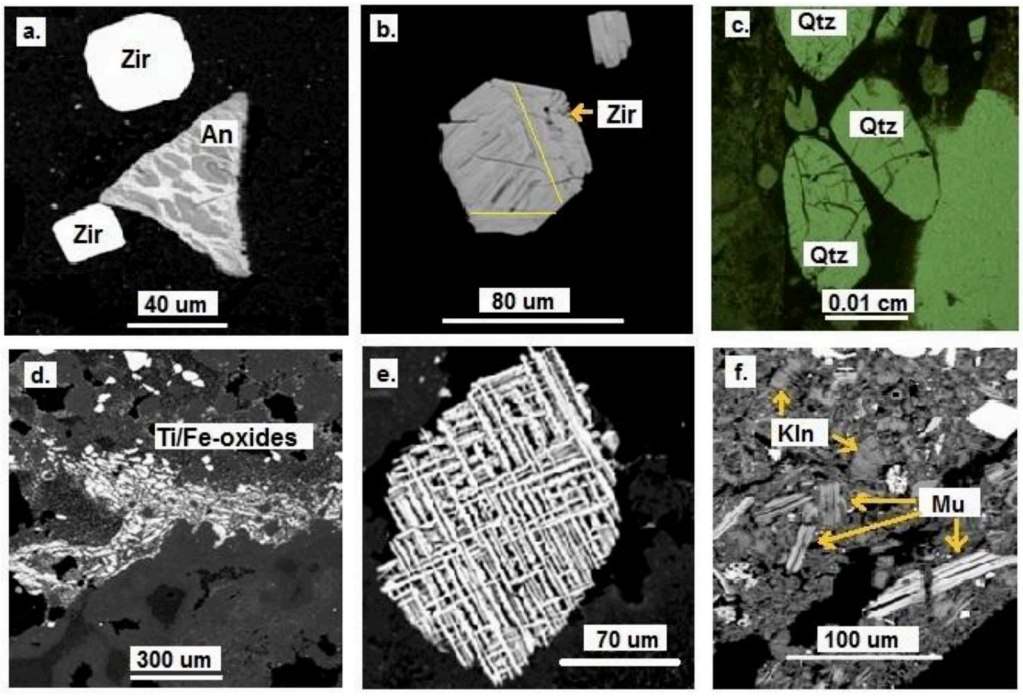


**Fig. 9.** (a) BSE image of euhedral zircon crystals (Zir) and a weathered anatase crystal (An) with dark grey Ti-Al-rich areas and light grey Fe-Ti-rich areas in KLB-11; (b) BSE image of zircon in KMG-11, showing re-growth textures at the bottom and upper right; (c) Rounded quartz grains in KLB-12 (PPL); (d) Accumulation of coarse- and fine-grained Fe-Ti-(Mn-)rich minerals in KLB-16; (e) Peculiar boxwork texture of a weathered Ti-oxide grain; (f) Cluster of kaolinite vermiculite stack (Kln) and muscovite flakes (Mu) in KMG-31.

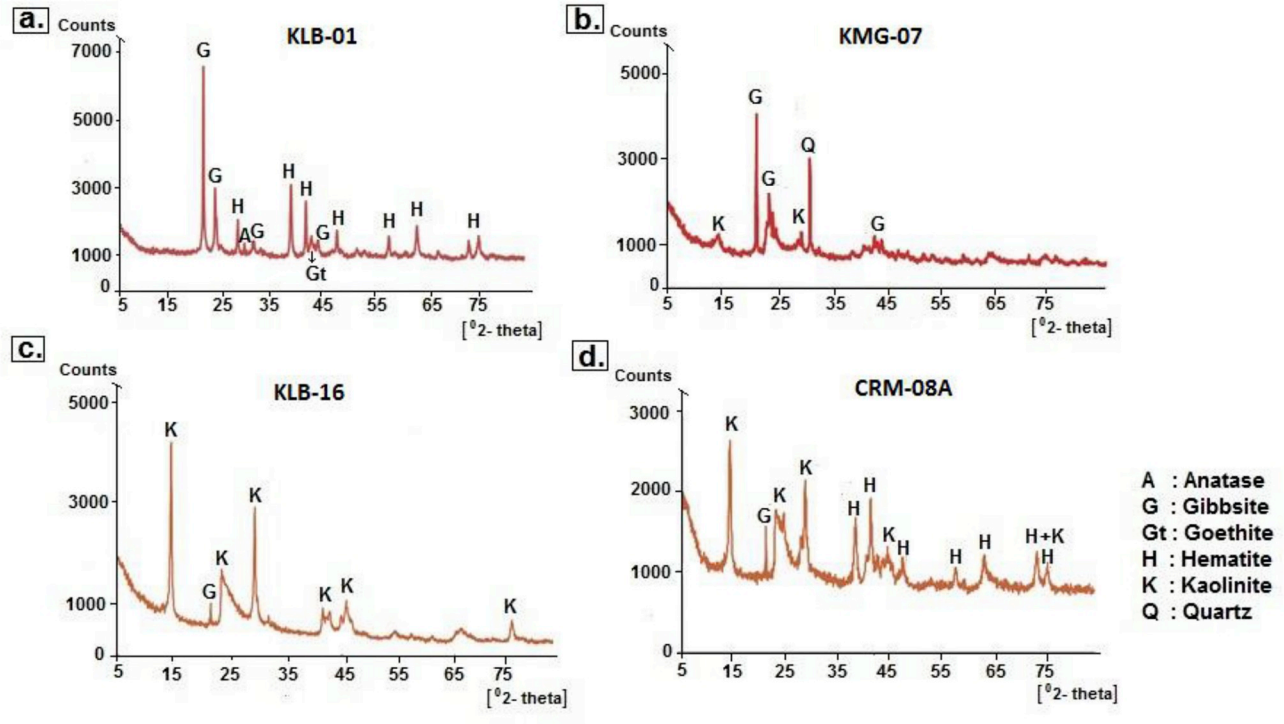


**Fig. 10.** (a) Representative XRD pattern for bauxite sample KLB-01 from the Klaverblad deposit; similar patterns were obtained from KMG and CRM bauxites; (b) XRD pattern from a grey quartz-rich lens (KMG-07); (c) XRD pattern of a white kaolin sample from the KLB deposit (KLB-16); (d) XRD pattern of a purple hematite-rich saprolite sample from the CRM deposit (CRM-08A). (For interpretation of the references to color in this figure legend, the reader is referred to the Web version of this article.)

*4.1.3. Coermotibo deposit*

The build-up of the Coermotibo deposit differs from the Successor and Lelydorp-1 sequences described above in the absence of a duricrust and its position mostly below a swamp. The ca. 40 m thick overburden is topped by a humus-rich layer that is thicker beneath the swamp and consists of alternating unconsolidated sand and clay layers of Miocene age, locally with intercalated peat lenses (Figs. 12b and 13a). Some of these sand layers are water-bearing (aquifers). The thickness of the heterogeneous gibbsite-rich bauxite horizon ranges between 0.2 m and 16 m, with a mean value of 6 m. Gibbsite is the dominant Al-phase in this deposit. Traces of boehmite and gibbsite linings in voids of clastic bauxite, suggesting multiple cycles of gibbsite formation, have also been reported (Van der Laan, 1998). Table 3 lists characteristics of the texturally different bauxite types, from the most (clayey) to the least

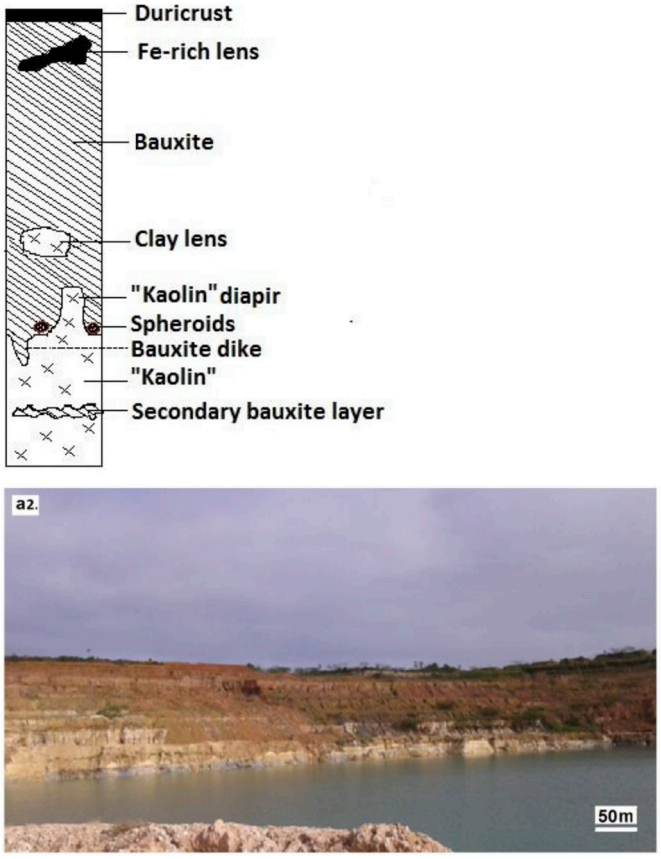


**Fig. 11.** a1. *Schematic representation of the lithofacies and structures in the Lelydorp-1 deposit.* Fig. 11. (a2) Overburden of the Lelydorp-1 deposit; (b) Iron-rich lens at the top of the bauxite layer (highlighted with red line); (c) Bauxite (BXT) dike surrounded by underlying saprolitic clays (KLN).; (d) Spheroid highlighted with red box.; (e) Coarse grained mica-rich underlying saprolitic clays with small spheroid highlighted in red box; (f) Cut slab of a spheroid displaying horizontal layering with perpendicular fractures; g) Banded underlying kaolinitic clay (kaolin). (For interpretation of the references to color in this figure legend, the reader is referred to the Web version of this article.)

(massive) abundant (Figs. 12b and 13a-b). At least 12 different sequences of lithofacies, found in crossing arrays of drill cores (cf., Fig. 12a and b; Monsels, 2004), demonstrate a conspicuous heterogeneity of this deposit, suggesting the local presence of lenses and effects from pre-burial erosion (e.g., presence of peat on bauxite, absence of kaolinitic bauxite in certain areas).

The predominantly grey hue of the Coermotibo bauxite is due to persistent reducing conditions, imposed by the overlying swamps, and the presence of marcasite ($FeS_2$) (Fig. 13a–c). The euhedral marcasite grains occasionally formed clusters (Fig. 13c), and indicate authigenic growth, similar to that of pyrite reported for this deposit and the Lelydorp 1,2,3 bauxites (Van der Laan, 1998). The post-diagenetic marcasite results from secondary sulfur enrichment, as has also been documented for other buried deposits where marshy sediments are in contact with bauxite (Valeton, 1972; Bárdossy and Aleva, 1990; Van der Laan, 1998). In these cases, pyrite crystals are commonly more abundant than marcasite, being more resistant to oxidation by iron-oxidizing bacteria than marcasite at low temperatures (Wang et al., 2007). Both marcasite and pyrite presumably formed in the reducing sulfur-rich environments of these deposits upon reaction of dissolved ferrous iron with reduced sulfur ($H_2S$) according to (Chan et al., 2012):

$$2H_2S_{(g)} + 0.5O_{2(g)} + Fe^{2+}{}_{(aq)} = Fe_2S_{(s)} + H_2O_{(l)} + 2H^{+}{}_{(aq)}$$

Despite the absence of a hard iron-rich duricrust on top of the Coermotibo bauxite horizon, a conspicuous red layer within the grey

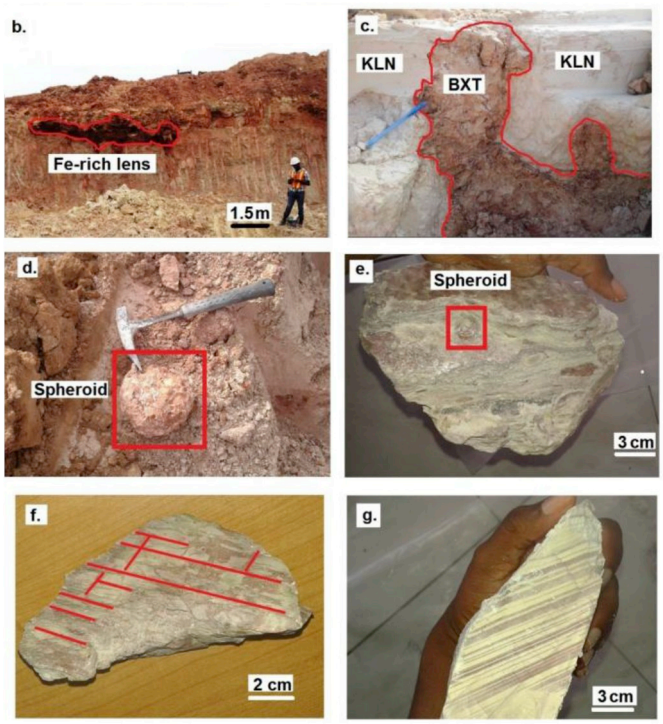


**Fig. 11.** (*continued*)

bauxite zone in the northern section of the deposit was identified as "groundwater laterite" (Schellmann, 1986), as its texture mirrors the surrounding clayey or clastic bauxite (Fig. 13b). It supposedly formed due to fluctuating groundwater, especially during dry periods when the level dropped and dissolved iron re-oxized (Schaetzl and Anderson, 2009).

Root-shaped concretions were present in the transition zone below the bauxite horizon (see section 4.1.1). The underlying white to grey clays (abundant kaolinite and halloysite) also contained mica flakes. The section across the MRJ district (Fig. 5) reveals that stratigraphic equivalents beneath the nearby bauxite deposits of Madoekas and Begi Gado crop out in the form of a muscovite- and kaolinite-rich sandstone and an up to 2 m thick quartz-pebble conglomerate layer, respectively (Figs. 4 and 13d-h).

### 4.2. Geochemistry

Average major element concentrations for the study areas are presented in Table 4, and a complete set of major and trace element data for the Successor Mines (KLB, CRM, KMG) in Table 5a.

#### 4.2.1. Major elements

All study areas contain Al-rich bauxite, with average $Al_2O_3$ concentrations ranging between 45 and 58 wt% (Table 4). The highest average $Al_2O_3$-content was found in the Coermotibo deposit (57.9 ± 5.3 wt%), which is further marked by significant amounts of sulfur (average $SO_3$ = 7.1 wt%). Silica contents are relatively high in the POL district (average $SiO_2$ = 12–23 wt%). The highest average silica concentration of 22.6 wt% in Lelydorp-1, probably reflects the large quantity of intercalated sand and kaolinite-rich layers and lenses. Iron contents are generally much higher in the Successor Mines (average $Fe_2O_3$ = 15–27 wt%) than in the other POL deposits and the MRJ area. Average $TiO_2$ contents show little variation between the different deposits.

The principal chemical differences between the bauxite deposits also appear in the ternary $Al_2O_3$-$Fe_2O_3$-$SiO_2$ classification diagrams (Schellman, 1986) of Fig. 14, constructed from Table 4 data. The

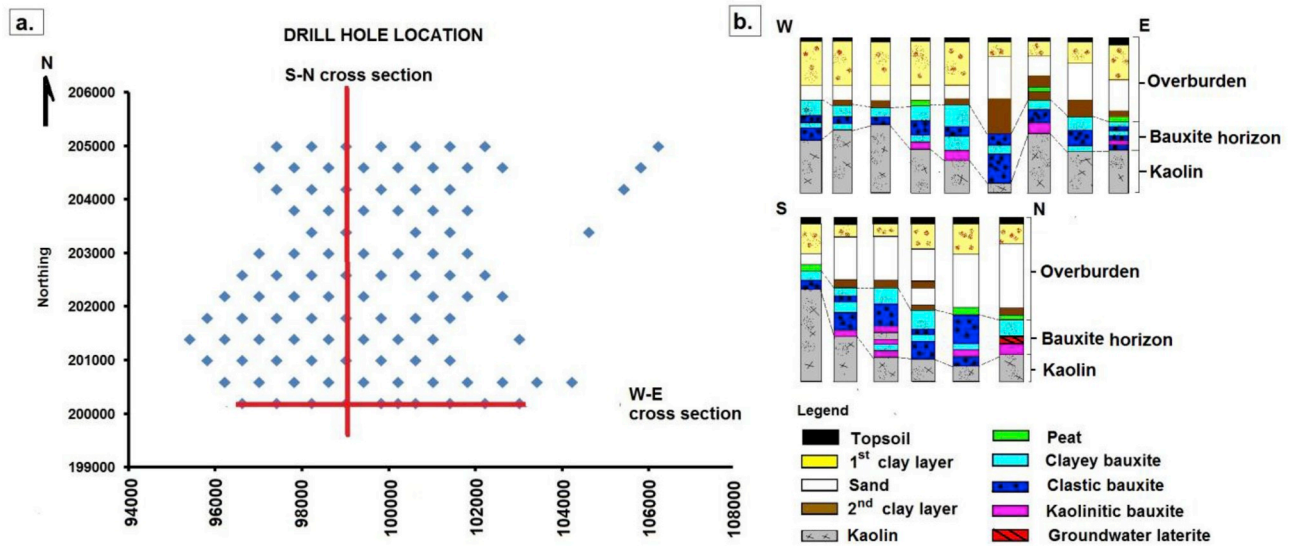


**Fig. 12.** (a) Schematic map of drill holes in the Coermotibo deposit from an exploration campaign in 2003; (b) Schematic EW and NS cross sections of the drillholes (not to scale), showing various lithofacies in the overburden and bauxite horizon with red (hematite) and grey-black (marcasite) staining, respectively (modified after Monsels, 2004). (For interpretation of the references to color in this figure legend, the reader is referred to the Web version of this article.)

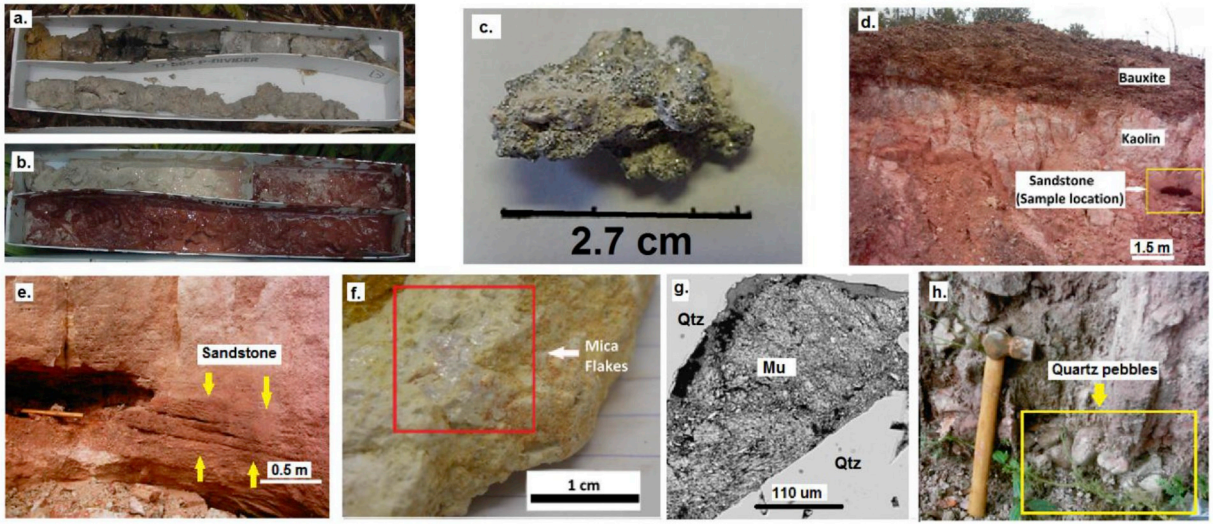


**Fig. 13.** (a) Drill cores from the Coermotibo deposit showing yellow clay from the overburden, black peat, and grey bauxite; (b) Transition from light-grey bauxite into an underlying red "groundwater laterite"; (c) Cluster of marcasite crystals recovered from the Coermotibo bauxite; (d) Residual bottom-layers of the lateritic weathering profile in the mined-out Madoekas Hill (Fig. 5a); (e) Close-up of the laminated sandstone in (d); (f) Cluster of mica flakes in the laminated sandstone of (e); (g) BSE image of a muscovite (Mu) cluster filling a void in a quartz grain (Qtz); (h) Quartz pebbles under the mined-out Begi Gado bauxite deposit. (For interpretation of the references to color in this figure legend, the reader is referred to the Web version of this article.)

**Table 3**
Textures and other properties of the Coermotibo bauxites arranged from most dominant to least observed.

| Bauxite texture | Consistency | Characteristics |
|---|---|---|
| Clayey | Plastic | Dominant ore type (Fig. 13a) |
| Slurry-like | Soft | Similar to wet clayey bauxite (under the groundwater table) (Fig. 13b) |
| Clastic or concretion-bearing | Friable | Consists of gibbsite-rich concretions |
| Kaolinitic | Plastic | Relatively $SiO_2$-rich and usually located in the transition zone between the bauxite and underlying kaolinitic clays; lacks in certain areas (Fig. 12b) |
| Massive | Hard | Generally located in dry high rises of the swampy area |

diagrams illustrate the iron-rich nature and overall high degree of lateritization of the Successor samples relative to the other deposits that all show fairly identical, $Al_2O_3$-rich and $Fe_2O_3$-poor signatures and a wider spread in degree of lateritization. This contrast points to differences in parent rock controls, weathering regimes and/or formation histories between the Successor Mines and the other deposits.

The distribution of $SiO_2$, $Al_2O_3$ and $Fe_2O_3$ in the investigated profiles (Fig. 15a) of the Successor deposits is linked to color and facies variations, which mirror relative abundances of the main minerals that host these oxides (gibbsite, kaolinite, hematite and goethite). The

**Table 4**
Average concentrations and standard deviations for main oxides and LOI, determined in grab samples from the studied Successor profiles (KLB, CRM, KMG) and available data sets from other POL and MRJ bauxites (Bauxite Institute Suriname and Suralco; East Group of Hills from Diko et al., 2001). Note that values represent overall averages and do not discriminate between various lithofacies that may be present within the deposits.

| Study area | Deposit | $SiO_2$ (wt.%) | $Al_2O_3$ (wt.%) | $TiO_2$ (wt.%) | $Fe_2O_3$ (wt.%) | LOI (wt.%) | n |
|---|---|---|---|---|---|---|---|
| **POL district** | | | | | | | |
| Successor deposits | Klaverblad | 6.0 ± 4.1 | 47.6 ± 9.4 | 1.8 ± 0.4 | 20.0 ± 16.5 | 24.3 ± 4.6 | 13 |
| | Caramacca | 11.3 ± 16.0 | 47.3 ± 10.4 | 2.2 ± 0.6 | 15.2 ± 14.8 | 23.8 ± 6.6 | 10 |
| | Kaaimangrasie | 4.6 ± 10.3 | 45.7 ± 12.1 | 2.0 ± 0.6 | 27.2 ± 12.7 | 20.2 ± 6.4 | 9 |
| | Lelydorp-1 | 22.6 ± 16.8 | 49.7 ± 10.3 | 2.3 ± 0.7 | 1.5 ± 0.8 | 23.8 ± 6.5 | 36 |
| | Kankantrie (Noord) | 17.4 ± 20.3 | 51.4 ± 12.7 | 2.1 ± 0.7 | 1.4 ± 1.5 | 26.5 ± 8.1 | 243 |
| | Para (Noord) | 12 .6 ± 10.4 | 53.9 ± 6.5 | 2.3 ± 0.8 | 2.1 ± 1.8 | 26.7 ± 4.9 | 287 |
| **MRJ district** | | | | | | | |
| | Coermotibo | 6.9 ± 9.3 | 57.9 ± 5.3 | 3.3 ± 0.4 | 2.1 ± 2.9 | 28.7 ± 4.3 | 44 |
| | East Group of Hills | 10.2 ± 11.7 | 49.4 ± 8.3 | 2.3 ± 0.6 | 12.1 ± 10.2 | 25.3 ± 5.6 | ca. 9250 |

**Table 5a**
Major oxide (XRF) and trace-element (LA-ICPMS) contents of samples from the Klaverblad lateritic weathering profile. n.d: not detected.

| *Sample* | Klaverblad lateritic weathering profile | | | | | | | | | | | |
|---|---|---|---|---|---|---|---|---|---|---|---|---|
| | KLB-01 | KLB-02 | KLB-03 | KLB-04 | KLB-05A | KLB-06 | KLB-07 | KLB-08 | KLB-09 | KLB-10 | KLB-11 | KLB-12 |
| *Depth (m)* | 0.25 | 0.75 | 1.25 | 1.75 | 2.25 | 2.75 | 3.25 | 4 | 4.75 | 5.5 | 6 | 6.75 |
| *Interval description* | Massive, breccia-like and cellular bauxite | | | | | | | | | Earthy, massive bauxite | White Al-rich layer | Earthy bauxite |
| *Color* | Brownish red, creme, yellow, dark brown, greyish black | | | | | | | | | Creme, yellow, pink | White | Creme, white, pink |
| **$SiO_2$ (wt.%)** | 3.48 | 3.15 | 2.01 | 6.45 | 4.30 | 3.24 | 2.61 | 3.88 | 11.35 | 11.71 | 9.15 | 14.07 |
| **$Al_2O_3$** | 44.68 | 47.64 | 50.94 | 33.28 | 38.03 | 32.83 | 40.19 | 46.88 | 53.16 | 56.44 | 57.94 | 55.26 |
| **$TiO_2$** | 1.55 | 2.03 | 1.97 | 1.52 | 1.47 | 1.23 | 1.08 | 1.49 | 1.83 | 1.96 | 2.40 | 2.31 |
| **$Fe_2O_3$** | 27.68 | 22.50 | 18.84 | 41.51 | 35.83 | 45.16 | 34.74 | 23.06 | 6.78 | 1.36 | 0.77 | 0.84 |
| **MnO** | 0.003 | 0.003 | 0.002 | 0.009 | 0.006 | 0.007 | 0.002 | 0.003 | 0.003 | 0.001 | 0.001 | 0.002 |
| **CaO** | 0.041 | 0.045 | 0.038 | 0.044 | 0.051 | 0.039 | 0.038 | 0.038 | 0.054 | 0.059 | 0.063 | 0.081 |
| **MgO** | 0.002 | 0.005 | n.d. | 0.027 | 0.022 | 0.010 | n.d. | 0.003 | n.d. | 0.004 | 0.002 | 0.011 |
| **$Na_2O$** | 0.039 | 0.036 | 0.035 | 0.023 | 0.023 | 0.036 | 0.034 | 0.096 | 0.027 | 0.109 | 0.056 | 0.101 |
| **$K_2O$** | 0.006 | 0.012 | 0.007 | 0.012 | 0.008 | 0.007 | 0.003 | 0.005 | 0.008 | 0.018 | 0.007 | 0.031 |
| **$P_2O_5$** | 0.16 | 0.18 | 0.12 | 0.20 | 0.24 | 0.23 | 0.12 | 0.12 | 0.17 | 0.13 | 0.17 | 0.17 |
| **LOI** | 22.37 | 24.39 | 26.03 | 16.92 | 20.02 | 17.19 | 21.17 | 24.42 | 26.63 | 28.22 | 29.45 | 27.13 |
| **Total** | 100 | 100 | 100 | 100 | 100 | 100 | 100 | 100 | 100 | 100 | 100 | 100 |
| **Sc (ppm)** | 13 | 13 | 10 | 16 | 18 | 16 | 8.3 | 9.0 | 13 | 11 | 8.5 | 9.1 |
| **V** | 405 | 364 | 249 | 568 | 624 | 771 | 357 | 233 | 194 | 76 | 107 | 88 |
| **Cr** | 155 | 176 | 124 | 248 | 237 | 222 | 129 | 96 | 189 | 144 | 210 | 181 |
| **Zn** | 16 | 12 | 12 | 19 | 21 | 20 | 12 | 11 | 12 | 17 | 14 | 19 |
| **As** | 20 | 24 | 13 | 36 | 30 | 33 | 15 | 15 | 5.0 | 1.8 | 2.0 | 3.0 |
| **Rb** | 0.4 | 0.7 | 0.4 | 0.8 | 0.6 | 0.3 | 0.1 | 0.1 | 0.3 | 0.6 | 0.3 | 1.2 |
| **Sr** | 38 | 83 | 34 | 59 | 68 | 45 | 30 | 28 | 122 | 147 | 201 | 197 |
| **Y** | 8.8 | 13 | 11 | 10 | 10 | 7.6 | 6.4 | 10 | 17 | 18 | 16 | 19 |
| **Zr** | 638 | 933 | 842 | 612 | 582 | 449 | 357 | 824 | 1363 | 1221 | 785 | 1143 |
| **Nb** | 30 | 41 | 33 | 33 | 30 | 28 | 25 | 34 | 50 | 43 | 49 | 49 |
| **Ba** | 26 | 47 | 23 | 38 | 51 | 26 | 21 | 19 | 51 | 60 | 95 | 90 |
| **La** | 17 | 38 | 20 | 24 | 23 | 16 | 15 | 18 | 45 | 60 | 71 | 69 |
| **Ce** | 30 | 77 | 29 | 48 | 45 | 31 | 28 | 25 | 90 | 123 | 174 | 171 |
| **Pr** | 3.7 | 9.1 | 3.5 | 5.8 | 5.3 | 3.6 | 3.2 | 3.0 | 10 | 13 | 18 | 16 |
| **Nd** | 15 | 35 | 13 | 23 | 21 | 14 | 11 | 11 | 39 | 51 | 71 | 56 |
| **Sm** | 3.2 | 7.3 | 2.5 | 4.7 | 5.0 | 3.3 | 2.2 | 2.1 | 7.5 | 9.3 | 14 | 11 |
| **Eu** | 0.70 | 1.3 | 0.56 | 0.91 | 0.99 | 0.73 | 0.50 | 0.40 | 1.4 | 1.9 | 2.9 | 2.4 |
| **Gd** | 2.4 | 4.7 | 2.2 | 3.3 | 3.6 | 2.3 | 1.6 | 1.6 | 4.8 | 6.9 | 9.2 | 8.8 |
| **Tb** | 0.37 | 0.63 | 0.34 | 0.44 | 0.49 | 0.33 | 0.26 | 0.26 | 0.72 | 0.93 | 1.2 | 1.1 |
| **Dy** | 2.2 | 3.7 | 2.3 | 2.6 | 2.8 | 1.9 | 1.4 | 1.8 | 4.2 | 5.0 | 6.1 | 6.0 |
| **Ho** | 0.42 | 0.65 | 0.47 | 0.46 | 0.47 | 0.32 | 0.30 | 0.40 | 0.78 | 0.87 | 0.85 | 0.97 |
| **Er** | 1.3 | 2.0 | 1.6 | 1.4 | 1.3 | 0.94 | 0.97 | 1.3 | 2.5 | 2.5 | 2.3 | 2.6 |
| **Yb** | 1.7 | 2.4 | 2.2 | 1.5 | 1.5 | 1.2 | 1.0 | 1.8 | 2.9 | 2.8 | 2.4 | 2.4 |
| **Lu** | 0.24 | 0.37 | 0.32 | 0.26 | 0.21 | 0.17 | 0.16 | 0.29 | 0.46 | 0.47 | 0.37 | 0.38 |
| **Hf** | 16 | 24 | 22 | 16 | 15 | 11 | 9.2 | 19 | 33 | 33 | 22 | 28 |
| **Ta** | 2.1 | 2.8 | 2.5 | 2.2 | 2.1 | 1.8 | 1.5 | 2.3 | 2.8 | 3.2 | 3.6 | 3.1 |
| **Pb** | 10 | 9.1 | 8.4 | 17 | 16 | 13 | 13 | 8.1 | 14 | 11 | 17 | 20 |
| **Th** | 85 | 73 | 64 | 106 | 123 | 111 | 58 | 63 | 116 | 88 | 123 | 69 |
| **U** | 6.5 | 7.3 | 5.1 | 7.1 | 7.6 | 5.7 | 3.5 | 4.8 | 7.9 | 7.3 | 9.0 | 6.3 |

Caramacca profile is most complete, as it shows a clear $Fe_2O_3$ enrichment in the duricrust as well as downward increasing $SiO_2$ and decreasing $Al_2O_3$ contents where the kaolin horizon appears. The Klaverblad and Kaaimangrasie profiles largely illustrate chemical variations within the bauxite horizon.

The erratic $Fe_2O_3$ trend in the KMG deposit (Fig. 15a) reflects its heterogeneous character and appears to be negatively correlated with $Al_2O_3$ and LOI. The presence of quartz-rich grey pockets (Fig. 8e,

**Table 5b**
Major oxide (XRF) and trace-element (LA-ICPMS) contents of samples from the Caramacca lateritic weathering profile. n.d: not detected.

| *Sample* | Caramacca lateritic weathering profile | | | | | | | | | | |
|---|---|---|---|---|---|---|---|---|---|---|---|
| | CRM-01 | CRM-01-02 | CRM-02 | CRM-03A | CRM-03B | CRM-04 | CRM-05 | CRM-06 | CRM-07 | CRM-08A | CRM-08B |
| *Depth (m)* | 0.25 | 0.75 | 2 | 3 | 3 | 4 | 4.5 | 5.25 | 6 | 6.75 | 6.75 |
| *Interval description* | Breccia-like | Earthy bauxite | | | | | | | Clayey bauxite | Kaolin | |
| *Color* | Brownish red, black | Pale yellow, creme | | | | Dark reddish brown, red, pale yellow, white | | | Creme, yellow | Purple, red, dark yellow | |
| **$SiO_2$ (wt.%)** | 0.71 | 0.93 | 15.23 | 6.04 | 5.38 | 1.47 | 0.73 | 1.46 | 42.59 | 38.05 | 33.03 |
| **$Al_2O_3$** | 34.82 | 60.84 | 49.32 | 59.21 | 59.86 | 50.18 | 42.78 | 44.22 | 38.25 | 33.11 | 29.71 |
| **$TiO_2$** | 1.67 | 2.24 | 2.50 | 2.81 | 2.93 | 2.93 | 1.66 | 2.19 | 1.53 | 1.39 | 1.08 |
| **$Fe_2O_3$** | 43.07 | 3.85 | 7.92 | 1.07 | 0.84 | 18.57 | 31.62 | 28.40 | 2.55 | 14.22 | 23.39 |
| **MnO** | 0.000 | 0.001 | 0.002 | 0.002 | 0.002 | 0.001 | 0.006 | 0.001 | 0.006 | 0.007 | 0.010 |
| **CaO** | 0.039 | 0.041 | 0.061 | 0.075 | 0.047 | 0.045 | 0.039 | 0.046 | 0.058 | 0.057 | 0.051 |
| **MgO** | 0.003 | n.d. | 0.036 | 0.011 | n.d. | n.d. | 0.010 | 0.008 | 0.026 | 0.057 | 0.038 |
| **$Na_2O$** | 0.034 | 0.017 | 0.050 | 0.029 | 0.012 | 0.021 | 0.022 | 0.027 | 0.041 | 0.049 | 0.042 |
| **$K_2O$** | 0.006 | 0.008 | 0.158 | 0.061 | 0.044 | 0.013 | 0.002 | 0.010 | 0.052 | 0.036 | 0.028 |
| **$P_2O_5$** | 0.33 | 0.12 | 0.22 | 0.11 | 0.11 | 0.19 | 0.09 | 0.24 | 0.07 | 0.06 | 0.08 |
| **LOI** | 19.31 | 31.95 | 24.51 | 30.58 | 30.78 | 26.59 | 23.03 | 23.40 | 14.81 | 12.97 | 12.54 |
| **Total** | 100 | 100 | 100 | 100 | 100 | 100 | 100 | 100 | 100 | 100 | 100 |
| **Sc (ppm)** | 9.0 | 5.5 | 13 | 7.8 | 10 | 10 | 6.3 | 9.2 | 8.7 | 12 | 12 |
| **V** | 417 | 165 | 779 | 136 | 136 | 456 | 172 | 291 | 72 | 139 | 173 |
| **Cr** | 369 | 183 | 453 | 470 | 514 | 324 | 159 | 308 | 126 | 83 | 116 |
| **Zn** | 9.5 | 10 | 20 | 45 | 18 | 12 | 12 | 9.3 | 15 | 15 | 28 |
| **As** | 52 | 7.4 | 17 | 4.0 | 3.7 | 30 | 26 | 42 | 4.3 | 22 | 17 |
| **Rb** | 0.2 | 0.2 | 7.8 | 2.9 | 2.1 | 0.4 | 0.1 | 0.4 | 2.7 | 1.8 | 1.9 |
| **Sr** | 18 | 26 | 102 | 78 | 82 | 37 | 13 | 46 | 53 | 10 | 11 |
| **Y** | 5.8 | 6.1 | 14 | 10 | 13 | 10 | 16 | 8.2 | 11 | 15 | 8.4 |
| **Zr** | 506 | 355 | 605 | 506 | 643 | 576 | 205 | 503 | 561 | 846 | 342 |
| **Nb** | 23 | 29 | 41 | 48 | 56 | 47 | 21 | 37 | 32 | 35 | 25 |
| **Ba** | 18 | 15 | 77 | 52 | 42 | 21 | 10 | 24 | 39 | 21 | 20 |
| **La** | 16 | 23 | 77 | 52 | 63 | 31 | 17 | 42 | 30 | 12 | 13 |
| **Ce** | 26 | 32 | 150 | 107 | 106 | 49 | 19 | 64 | 55 | 14 | 14 |
| **Pr** | 2.5 | 3.3 | 14 | 9.4 | 10 | 4.7 | 2.1 | 5.7 | 5.1 | 1.4 | 1.7 |
| **Nd** | 7.2 | 10 | 41 | 27 | 31 | 15 | 6.7 | 16 | 16 | 4.3 | 5.5 |
| **Sm** | 1.1 | 1.5 | 5.4 | 3.4 | 3.8 | 1.9 | 1.3 | 2.0 | 2.6 | 0.94 | 1.0 |
| **Eu** | 0.20 | 0.25 | 0.83 | 0.64 | 0.66 | 0.41 | 0.31 | 0.31 | 0.46 | 0.16 | 0.19 |
| **Gd** | 0.83 | 0.95 | 3.1 | 1.7 | 2.3 | 1.4 | 1.5 | 1.3 | 1.6 | 1.2 | 0.93 |
| **Tb** | 0.13 | 0.15 | 0.40 | 0.26 | 0.32 | 0.20 | 0.21 | 0.19 | 0.26 | 0.24 | 0.18 |
| **Dy** | 1.0 | 1.1 | 2.7 | 1.9 | 2.5 | 1.7 | 1.5 | 1.4 | 1.9 | 2.1 | 1.5 |
| **Ho** | 0.22 | 0.25 | 0.58 | 0.36 | 0.53 | 0.37 | 0.32 | 0.31 | 0.43 | 0.56 | 0.34 |
| **Er** | 0.81 | 0.82 | 2.0 | 1.3 | 1.8 | 1.2 | 1.0 | 1.1 | 1.5 | 2.0 | 1.1 |
| **Yb** | 1.1 | 1.1 | 2.3 | 1.6 | 2.3 | 1.7 | 1.0 | 1.4 | 2.1 | 2.8 | 1.5 |
| **Lu** | 0.17 | 0.17 | 0.36 | 0.26 | 0.37 | 0.26 | 0.16 | 0.23 | 0.35 | 0.47 | 0.26 |
| **Hf** | 13 | 10 | 18 | 14 | 18 | 15 | 5.7 | 14 | 15 | 21 | 10 |
| **Ta** | 1.7 | 2.3 | 3.5 | 3.5 | 4.2 | 3.5 | 1.6 | 2.8 | 2.2 | 2.3 | 1.8 |
| **Pb** | 10 | 10 | 40 | 33 | 26 | 12 | 7.3 | 22 | 21 | 10 | 17 |
| **Th** | 107 | 65 | 117 | 106 | 137 | 104 | 39 | 99 | 46 | 36 | 40 |
| **U** | 3.4 | 3.0 | 4.8 | 7.1 | 4.5 | 4.4 | 2.3 | 3.7 | 3.5 | 4.3 | 3.2 |

sample KMG-07) adds to the heterogeneity of the deposit and explains the $SiO_2$ peak at 3.5 m. Vertical major-element trends in the other study areas (Fig. 15b) appear smoother than those of the Successor deposits (Fig. 15a). This is partly due to the difference in sampling strategy, since individual samples from the exploration or check-drill campaigns (data set from Bauxite Institute of Suriname and Suralco) represented relatively large intervals, and drill cuttings may have obscured small-scale lithofacies changes. Also, in absence of accompanying petrographic descriptions, a subdivision into distinct lithofacies cannot be made, but exploration practices make it likely that these profiles only include the bauxite horizons.

In all of the study areas, the vertical $SiO_2$ distribution shows relatively little fluctuation except for some local anomalies and increasing tendencies towards the top and/or bottom in some of the profiles. The $SiO_2$ abundance is largely controlled by kaolinite, which is the dominant silica-bearing phase in the transition zone and underlying saprolitic clays. Occasionally quartz grains (e.g in grey lenses) also influence the $SiO_2$ content. The $SiO_2$ increases towards the top of the weathering profiles of Lelydorp-1, Para (Noord), and Kankantrie (Noord) (Fig. 14b) is probably due to kaolinitization of the bauxite (*in-situ* $SiO_2$ source) or resilication (external $SiO_2$ origin), which has also been reported for other POL deposits as well as for Brazilian bauxites (Janssen, 1979; Bárdossy and Aleva, 1990; Carvalho et al., 1997; Mateus et al., 2017). The silica supply may come from dissolving quartz grains in the bauxite (similar to those of the Successor Mines, Fig. 9c) or from infiltrating silica-rich solutions derived from the overburden.

Major and trace-element abundances normalized to upper continental crust (UCC; Rudnick and Gao, 2004) can be used to explore the relative (im)mobility of elements in the bauxite profiles of the Successor deposits (Fig. 16). In the upper parts, silica and other soluble elements (monovalent and bivalent) are highly depleted, and an inverse correlation between $Al_2O_3$ and $Fe_2O_3$ largely reflects the proportions of gibbsite and goethite. In lower parts, where $SiO_2$ concentrations tend to be higher.due to the presence of kaolinite, $Al_2O_3$ and $Fe_2O_3$ contents are

**Table 5c**
Major oxide (XRF) and trace-element (LA-ICPMS) contents of samples from the Kaaimangrasie lateritic weathering profile. n.d: not detected.

| *Sample* | Kaaimangrasie lateritic weathering profile | | | | | | | | |
|---|---|---|---|---|---|---|---|---|---|
| | KMG-01 | KMG-02 | KMG-04 | KMG-05 | KMG-06 | KMG-07 | KMG-08 | KMG-09 | KMG-10 |
| *Depth (m)* | 0.5 | 1 | 2 | 2.5 | 3 | 3.5 | 4 | 4.5 | 5 |
| *Interval description* | Massive, breccia-like and cellular bauxite | | | | | Grey Si-rich lens | Massive, breccia-like bauxite | | Earthy- clayey bauxite |
| *Color* | Dark brownish red, dark red, black, creme | | | | | Grey | Creme, brownish red | | Creme |
| **$SiO_2$ (wt.%)** | 0.49 | 0.48 | 0.45 | 0.97 | 1.46 | 32.05 | 1.13 | 3.07 | 4.95 |
| **$Al_2O_3$** | 45.69 | 38.97 | 49.80 | 34.10 | 47.75 | 36.30 | 36.08 | 48.39 | 60.02 |
| **$TiO_2$** | 2.08 | 1.86 | 2.86 | 1.21 | 1.76 | 1.75 | 1.54 | 1.90 | 2.97 |
| **$Fe_2O_3$** | 27.35 | 42.71 | 20.02 | 44.62 | 22.62 | 11.53 | 41.63 | 19.92 | 0.98 |
| **MnO** | n.d. | n.d. | 0.001 | 0.003 | 0.001 | 0.003 | n.d. | 0.001 | 0.001 |
| **CaO** | 0.035 | 0.036 | 0.039 | 0.038 | 0.098 | 0.057 | 0.035 | 0.037 | 0.046 |
| **MgO** | n.d. | n.d. | n.d. | 0.007 | n.d. | 0.260 | 0.008 | 0.003 | n.d. |
| **$Na_2O$** | 0.023 | 0.022 | 0.021 | 0.039 | 0.036 | 0.113 | 0.033 | 0.045 | 0.023 |
| **$K_2O$** | 0.007 | 0.008 | 0.006 | 0.006 | 0.025 | 0.801 | 0.016 | 0.047 | 0.019 |
| **$P_2O_5$** | 0.08 | 0.17 | 0.17 | 0.10 | 0.17 | 0.10 | 0.16 | 0.20 | 0.10 |
| **LOI** | 24.24 | 15.75 | 26.64 | 18.91 | 26.08 | 17.03 | 19.37 | 26.39 | 30.89 |
| **Total** | 100 | 100 | 100 | 100 | 100 | 100 | 100 | 100 | 100 |
| **Sc (ppm)** | 5.3 | 6.4 | 5.6 | 6.3 | 7.3 | 16 | 10 | 8.5 | 11 |
| **V** | 115 | 225 | 207 | 120 | 483 | 460 | 679 | 517 | 92 |
| **Cr** | 102 | 206 | 191 | 132 | 159 | 217 | 460 | 267 | 246 |
| **Zn** | 4.6 | 5.4 | 13 | 13 | 49 | 63 | 13 | 26 | 21 |
| **As** | 6.8 | 14 | 17 | 11 | 30 | 25 | 22 | 19 | 2.5 |
| **Rb** | 0.2 | 0.3 | 0.3 | 0.2 | 1.2 | 51 | 0.9 | 2.7 | 0.8 |
| **Sr** | 11 | 9.3 | 12 | 12 | 22 | 62 | 14 | 23 | 48 |
| **Y** | 5.5 | 3.7 | 4.8 | 8.4 | 7.3 | 18 | 5.5 | 7.2 | 18 |
| **Zr** | 264 | 190 | 265 | 212 | 349 | 356 | 326 | 372 | 1153 |
| **Nb** | 27 | 22 | 33 | 19 | 34 | 34 | 26 | 37 | 55 |
| **Ba** | 10 | 10 | 13 | 11 | 50 | 199 | 16 | 38 | 29 |
| **La** | 15 | 13 | 18 | 14 | 23 | 50 | 17 | 25 | 51 |
| **Ce** | 20 | 15 | 22 | 20 | 27 | 79 | 21 | 39 | 71 |
| **Pr** | 2.0 | 1.7 | 2.3 | 2.1 | 3.1 | 8.3 | 2.3 | 3.6 | 6.8 |
| **Nd** | 6.6 | 5.2 | 6.4 | 7.0 | 10 | 28 | 7.0 | 10 | 20 |
| **Sm** | 1.0 | 0.81 | 0.95 | 1.2 | 1.5 | 4.5 | 1.0 | 1.5 | 3.4 |
| **Eu** | 0.21 | 0.13 | 0.33 | 0.29 | 0.26 | 0.78 | 0.22 | 0.28 | 0.48 |
| **Gd** | 0.80 | 0.55 | 0.69 | 1.2 | 1.1 | 3.3 | 0.72 | 1.1 | 2.3 |
| **Tb** | 0.14 | 0.10 | 0.12 | 0.18 | 0.18 | 0.48 | 0.13 | 0.16 | 0.36 |
| **Dy** | 1.0 | 0.70 | 0.87 | 1.4 | 1.4 | 3.4 | 1.0 | 1.2 | 3.0 |
| **Ho** | 0.22 | 0.14 | 0.18 | 0.32 | 0.27 | 0.68 | 0.22 | 0.28 | 0.63 |
| **Er** | 0.77 | 0.51 | 0.67 | 0.93 | 0.96 | 2.3 | 0.76 | 0.90 | 2.5 |
| **Yb** | 0.95 | 0.65 | 0.89 | 0.90 | 1.1 | 2.5 | 1.1 | 1.2 | 3.3 |
| **Lu** | 0.17 | 0.10 | 0.14 | 0.15 | 0.19 | 0.37 | 0.15 | 0.19 | 0.55 |
| **Hf** | 7.9 | 5.5 | 7.6 | 5.7 | 10 | 11 | 10 | 10 | 32 |
| **Ta** | 2.1 | 1.6 | 2.5 | 1.4 | 2.4 | 2.5 | 2.0 | 2.6 | 4.2 |
| **Pb** | 6.4 | 8.7 | 8.0 | 6.9 | 14 | 42 | 15 | 21 | 26 |
| **Th** | 44 | 62 | 54 | 35 | 49 | 51 | 101 | 78 | 107 |
| **U** | 1.9 | 1.7 | 2.4 | 1.5 | 3.5 | 4.4 | 2.4 | 3.1 | 6.1 |

lower, in agreement with less extensive removal of soluble components. A few $SiO_2$-poor samples near the bottom of some of the drill holes of the Kankantrie (Noord) and Para (Noord) deposits probably correspond to a second bauxite layer or “dike”, which has also been observed in the Lelydorp-1 deposit (Fig. 11c).

The mobility of *iron* is evidenced by its stronger accumulation in the duricrust relative to aluminium, and by numerous void fillings by goethite and hematite, as well as locally abundant iron mottles, nodules and stains (Fig. 8c,e). Staining of the overall white, iron-poor kaolin in lower parts of the profiles can also be attributed to iron enrichment, as kaolinite may incorporate this element in its structure (Tardy, 1997) (Figs. 8a, 10c and 10d). The mobility of Fe (and Al) in bauxite is influenced by organic complexing and effective leaching processes of percolating pore waters where pH-Eh conditions play a significant role (Huang and Keller, 1972; Boulangé, 1984; Tardy and Nahon, 1985; Bárdossy and Aleva, 1990; Schwertmann, 1991; Laskou and Economou-Eliopoulos, 2007; Ling et al., 2017).

Despite the generally assumed immobility of *titanium*, based on the resistance of Ti-bearing minerals to weathering and low solubility of Ti in water, micro-textures such as various intergrowths of Ti-Fe-oxides rimming distinct microscopic domains, point to mobility of both elements (Fig. 9d) at least on a small scale. Cornu et al. (1999) documented evidence for significant titanium mobility in soil profiles in the tropical environment of central Amazonia, which was likely linked to the complexing capacity of organic compounds and acidic conditions. Valeton (1972) suggested that Ti can also be mobilized as colloidal hydrated titanium oxides which may be ultimately dehydrated to form fine-grained anatase, which requires some re-distribution at least on (sub)centimeter scale. There is no obvious trend in the UCC-normalized profiles for Ti, which is predominantly stored in anatase, rutile, ilmenite and their alteration products.

Chemical indicators confirm that the investigated bauxite deposits represent advanced stages of weathering. Values for the Chemical Index of Alteration [CIA = 100 x $Al_2O_3/(Al_2O_3 + CaO + Na_2O + K_2O)$; Nesbitt and Young, 1982; Wei et al., 2014] are > 99 for all samples from the Successor deposits, consistent with efficient removal of Ca, Na and K, which is also evident in Table 5a–c.

### 4.2.2. Trace elements

Inspection of the vertical profiles (Fig. 14a and Table 5a–d) and

**Table 5d**
Major oxide (XRF) and trace-element (LA-ICPMS) contents of supplementary samples from the Successor deposits n.d: not detected.

| Supplementary samples | | | | | | | |
|---|---|---|---|---|---|---|---|
| *Sample* | KLB-13 | KLB-14 | KLB-17 | KLB-18 | KLB-19 | CRM-32 | KMG-16 |
| *Depth (m)* | 7.5 | ± 8 | ± 9.5 | ± 10 | ± 10.5 | ± 1.0 | ± 10.5 |
| *Interval description* | Earthy bauxite | | Cellular bauxite + burrows | Kaolin | Rootshaped concretion | Black Fe-rich lens | Kaolin |
| *Color* | creme, white, pink | Pink, creme, white | creme, pink,orange | purple | white, pink | reddish black | grey-pink |
| $SiO_2$ (wt.%) | 2.64 | 3.79 | 3.80 | 4.59 | 43.82 | 0.68 | 40.50 |
| $Al_2O_3$ | 61.29 | 60.67 | 58.35 | 57.35 | 38.51 | 21.43 | 40.52 |
| $TiO_2$ | 2.38 | 2.22 | 5.42 | 5.79 | 2.12 | 0.63 | 1.37 |
| $Fe_2O_3$ | 0.87 | 0.76 | 2.19 | 2.68 | 0.81 | 63.02 | 1.13 |
| MnO | 0.001 | 0.002 | 0.013 | 0.018 | 0.006 | n.d. | 0.004 |
| CaO | 0.083 | 0.077 | 0.073 | 0.069 | 0.099 | 0.037 | 0.059 |
| MgO | 0.081 | 0.111 | n.d. | n.d. | 0.040 | 0.027 | 0.027 |
| $Na_2O$ | 0.377 | 0.504 | 0.049 | 0.030 | 0.132 | 0.046 | 0.042 |
| $K_2O$ | 0.062 | 0.065 | 0.076 | 0.069 | 0.066 | 0.011 | 0.052 |
| $P_2O_5$ | 0.13 | 0.12 | 0.29 | 0.19 | 0.07 | 0.16 | 0.06 |
| LOI | 32.08 | 31.68 | 29.75 | 29.21 | 14.32 | 13.95 | 16.25 |
| Total | 100 | 100 | 100 | 100 | 100 | 100 | 100 |
| Sc (ppm) | 0.6 | 0.8 | 31 | 30 | 14 | 6.2 | 9.1 |
| V | 5.3 | 7.3 | 231 | 209 | 78 | 56 | 66 |
| Cr | 5.2 | 6.4 | 267 | 272 | 144 | 56 | 110 |
| Zn | 4.3 | 5.2 | 21 | 26 | 48 | 15 | 30 |
| As | 0.94 | 1.5 | 8.3 | 10 | 2.0 | 75 | n.d. |
| Rb | 4.9 | 6.9 | 2.1 | 2.6 | 2.4 | 0.3 | 3.2 |
| Sr | 7.1 | 12 | 612 | 277 | 52 | 8.4 | 21 |
| Y | 1.1 | 1.7 | 82 | 82 | 31 | 7.0 | 14 |
| Zr | 9.1 | 14 | 4016 | 3636 | 1769 | 495 | 818 |
| Nb | 0.62 | 0.87 | 123 | 136 | 50 | 9.2 | 33 |
| Ba | 13 | 20 | 304 | 129 | 54 | 5.9 | 29 |
| La | 1.5 | 2.2 | 311 | 138 | 29 | 8.3 | 20 |
| Ce | 3.0 | 4.1 | 435 | 209 | 53 | 10 | 26 |
| Pr | 0.35 | 0.48 | 49 | 24 | 5.7 | 0.93 | 2.5 |
| Nd | 1.4 | 1.9 | 196 | 93 | 19 | 2.7 | 7.1 |
| Sm | 0.27 | 0.39 | 37 | 18 | 3.6 | 0.48 | 1.4 |
| Eu | 0.05 | 0.07 | 7.3 | 3.5 | 0.8 | 0.08 | 0.29 |
| Gd | 0.24 | 0.34 | 21.7 | 13.4 | 3.5 | 0.48 | 1.2 |
| Tb | 0.03 | 0.05 | 2.8 | 2.2 | 0.6 | 0.12 | 0.24 |
| Dy | 0.23 | 0.33 | 17 | 16 | 5.0 | 1.1 | 2.0 |
| Ho | 0.04 | 0.06 | 3.2 | 3.4 | 1.2 | 0.26 | 0.51 |
| Er | 0.13 | 0.19 | 10 | 11 | 4.1 | 1.0 | 1.8 |
| Yb | 0.12 | 0.19 | 14 | 15 | 5.7 | 1.4 | 2.5 |
| Lu | 0.02 | 0.03 | 2.3 | 2.4 | 0.99 | 0.22 | 0.40 |
| Hf | 0.26 | 0.41 | 100 | 97 | 50 | 13 | 20 |
| Ta | 0.05 | 0.07 | 8.5 | 10 | 3.9 | 0.68 | 2.2 |
| Pb | 1.6 | 2.1 | 70 | 49 | 18 | 4.5 | 14 |
| Th | 0.49 | 0.72 | 187 | 181 | 56 | 17 | 44 |
| U | 0.11 | 0.16 | 15 | 16 | 7.4 | 2.0 | 3.8 |

UCC-normalized trends (Fig. 16) provides important clues concerning parameters that controlled the behaviour of trace elements in the Successor deposits. The UCC-normalized plots of the three Successor deposits (Fig. 16) are fairly similar, with positive LREE, MREE and HFSE anomalies (except Pb and U). The REE section of the UCC-normalized patterns is not uniform, as it is upward concave for CRM and KMG, and downward concave for KLB (Fig. 16). The KLB patterns illustrate the existence of systematic variations in trace-element concentrations as a function of $SiO_2$ contents. Virtually all trace elements (REE, Y, HFSE, Sr) of the KLB samples are enriched in the layers with $SiO_2 > 5$ wt%, whereas the Fe-rich top part with $SiO_2 <$ wt.5% has highest contents of As, V, Sc. This association can be ascribed to the presence of placer-like accumulations of heavy minerals in the bottom layers of the profile and, to a lesser extent, absorption of these trace elements onto clay minerals. Typical heavy mineral hosts of trace elements are zircon (Zr, Nb, Hf, Ta, Th and U) anatase (Ti, V and Zr), ilmenite (Cr, V, Ti), titanite (Ti, Nb, Mg, V), and xenotime for LREE and MREE (Laveuf and Cornu, 2009), which have almost all been identified in the investigated deposits. Only xenotime has not been found so far but this mineral has been reported from the other bauxite deposits from the POL bauxite district (Aleva et al., 1969; Krook, 1969a). Anatase can accommodate many of these elements in its structure during neomineralisation (Valeton, 1972). Because accessory minerals as these tend to concentrate almost all “immobile” trace elements, their association in the precursor material(s) and stability during the weathering process largely determines the trace-element signatures of bulk samples, as has been demonstrated for the lateritic plateau bauxites of Suriname (Monsels and Van Bergen, 2017) and other lateritic or karst bauxites (e.g., Ling et al., 2017; Ahmadnejad et al., 2017). Given their generally residual behaviour, the observed relative enrichment of Cr, Nb, Ti, Th, V, Y and Zr during bauxitization is expected (Goldschmidt, 1937, 1954; Logemerac, 1969, and references therein), while concentration variations can be ascribed to internal heterogeneity of accessory minerals in the precursor material, possibly with additional effects from post-bauxitization processes such as leaching, ferruginisation and resilication (Carvalho et al., 1997).

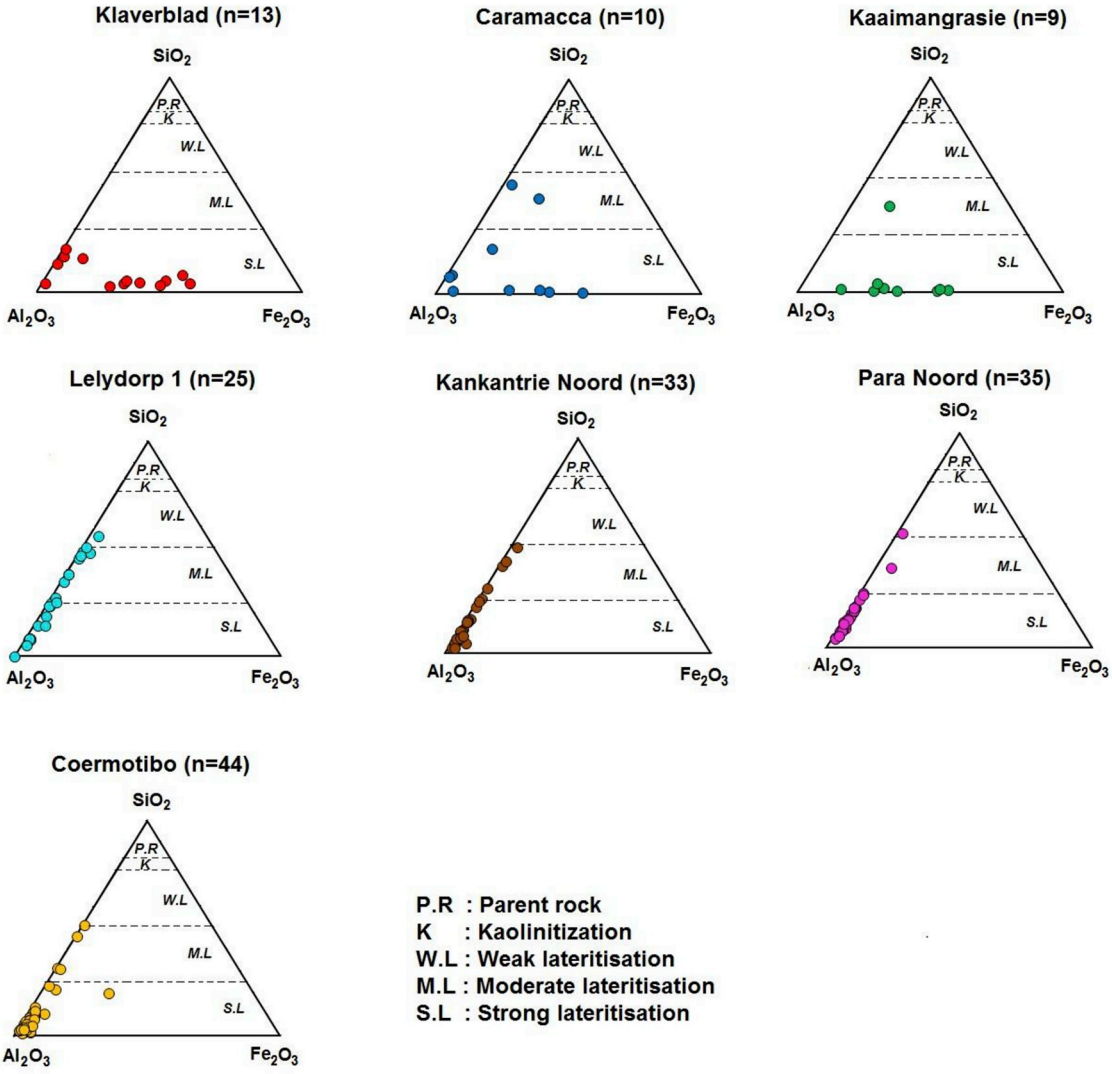


**Fig. 14.** *Triangular plots (based on Schellmann, 1983,1986,) depicting the degree of lateritization in all the study areas.*

*4.2.3. Possible relationship between bauxite and underlying saprolitic clay*

The trace-element data provide new clues concerning the relationship between bauxite and underlying sediments, which has remained unclear so far. A long-standing point of discussion is whether the bauxites developed on arkosic sandstone interlayed with clayey sediments (Aleva, 1965; Aleva et al., 1969; Krook, 1969a,b, 1979; Wong et al., 1998, 2009 and references therein) or on the kaolinitic clays that frequently occur below the deposits (Bakker et al., 1953; Van Kersen, 1956; Moses and Michell, 1963; Doeve and Groeneveld Meijer, 1963). A comparison of UCC-normalized REE patterns of the Successor bauxites and underlying kaolin is helpful for this purpose (Fig. 17). Parallel REE patterns would argue in favour of a common genetic history, but only if fractionation during the weathering process can be excluded. In all cases, the kaolin tends to deviate significantly from the bauxite, either in the shape of the trends or in concentration levels of the REE (Fig. 17). The KLB kaolin (KLB-18) is marked by REE enrichment and a relatively flat pattern. While the HREE are parallel, the LREE do not show the "bulge" around Sm, seen in the majority of the bauxite samples. Also, the kaolin composition seems to follow an overall increase in REE contents towards the bottom of the KLB profile (Fig. 17). These observations are difficult to reconcile with weathering-induced modification of an originally homogeneous package of sedimentary parent rock. Accumulation of REE, leached from overlying layers, is conceivable but is unlikely to have affected the HREE, because this group was probably immobile as it is proably largely stored in zircon. Downward increasing Zr and Hf contents are consistent with larger amounts of zircon near the bottom of the profile. The geochemical signatures thus point to compositional variation of sediment layers, which argues against a direct genetic relationship between bauxite and the underlying kaolinitic clay layers, either in a uniform weathering profile or in a scenario wherein bauxite formed on a parent of kaolinitic clay. This interpretation for KLB is tentative because the kaolin sample (KLB-18) was not taken from the same location as that of the vertical profile, and lateral variation within the deposit cannot be excluded. In the KMG and CRM profiles the REE trends of the underlying kaolin and bauxite samples are also not entirely parallel. The shapes of the HREE parts largely coincide, but the LREE deviate and are relatively depleted in the CRM profile. Although the LREE are apparently more affected by mobility (leaching) during weathering than the HREE, it is difficult to envisage why they would have been preferentially removed from the kaolin, whereas typically mobile elements such as Si, Ca, Na, K, Rb are relatively enriched compared to the bauxite samples (Fig. 16). Again, for the KMG the comparison should be considered with care since the kaolin sample (KMG-16), comes from a different location than the profile. Other kaolin samples from the same deposit (KMG-32, KMG-33, not shown) display the same REE pattern albeit at different locations.

The divergent geochemical trend of sample KMG-07 (Fig. 17) can be explained by its different composition, as this sample was located in a

grey $SiO_2$-rich lens (Fig. 8e) that contained numerous quartz grains and probably accommodated a relatively large amount of weathering resistant heavy minerals.

Because all of the CRM samples were collected in the same continuous vertical profile, the dissimilar REE patterns suggests that the kaolin in the bottom part (CRM-08A and CRM-08B) is not the parent rock of the overlying bauxite, nor can they be seen as products of a single weathering process that acted on a single precursor sediment. Instead, the REE signatures likely reflect heterogeneity in the original sequence of sediments (which may have experienced a different

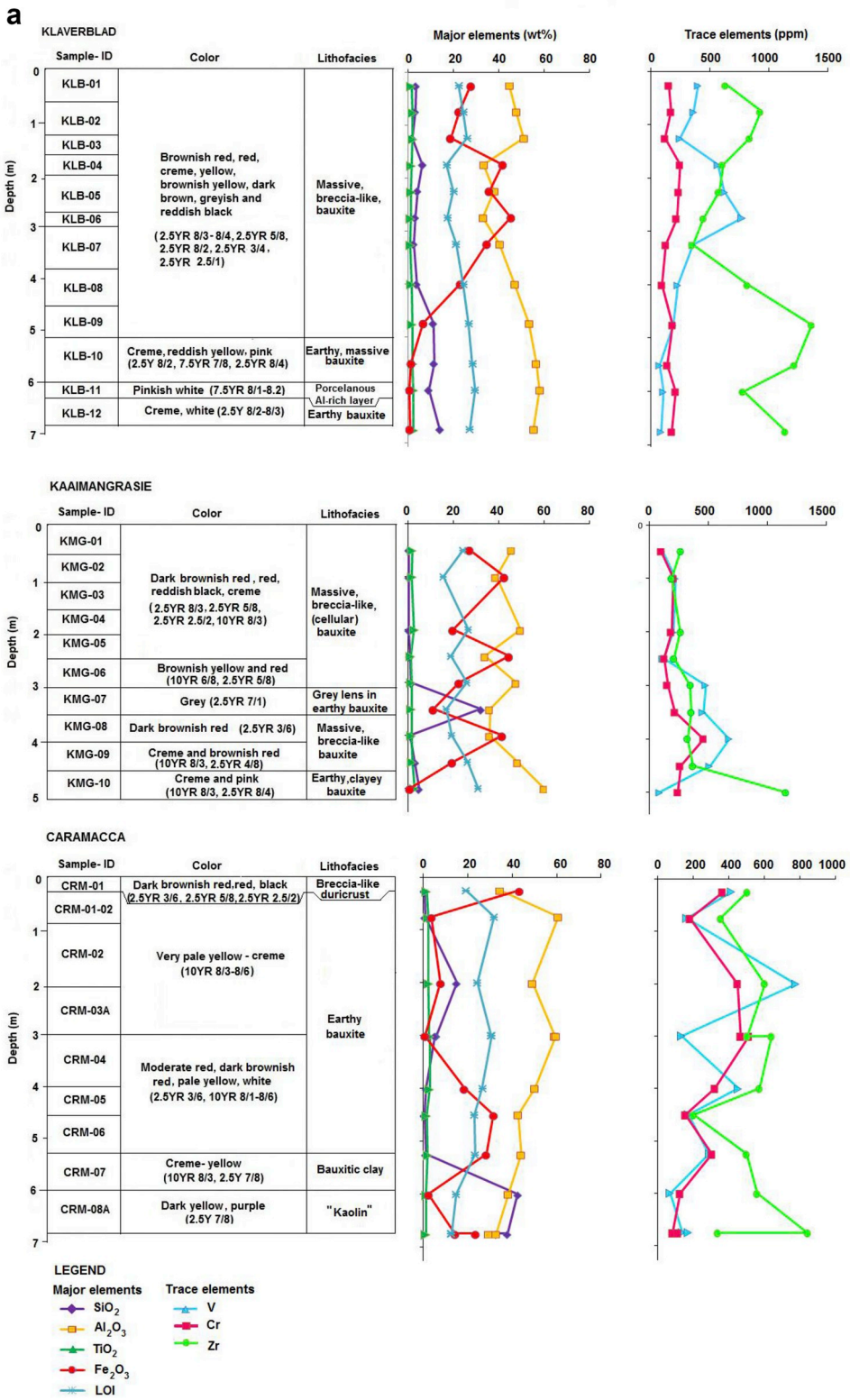


**Fig. 15.** a. *Vertical changes in selected major and trace element concentrations of the Successor deposits (KLB, KMG, CRM), based on field samples.* Fig. 15**b.** Vertical changes in major element concentrations in weathering profiles of Lelydorp-1, Para (Noord), Kankantrie (Noord) and Coermotibo, based on samples from exploration drilling (Suralco and Bauxite Institute of Suriname).

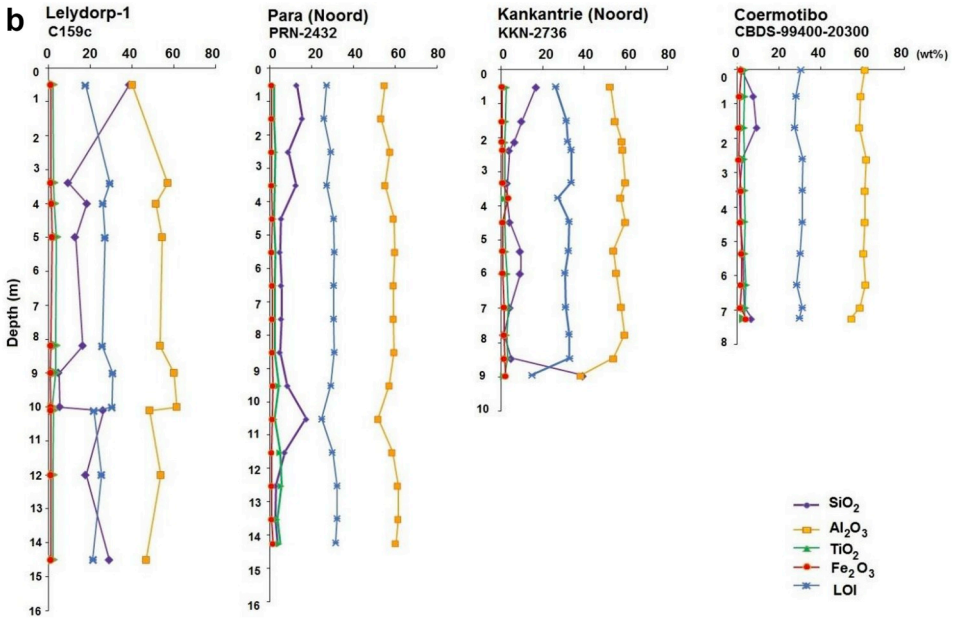


**Fig. 15.** (*continued*)

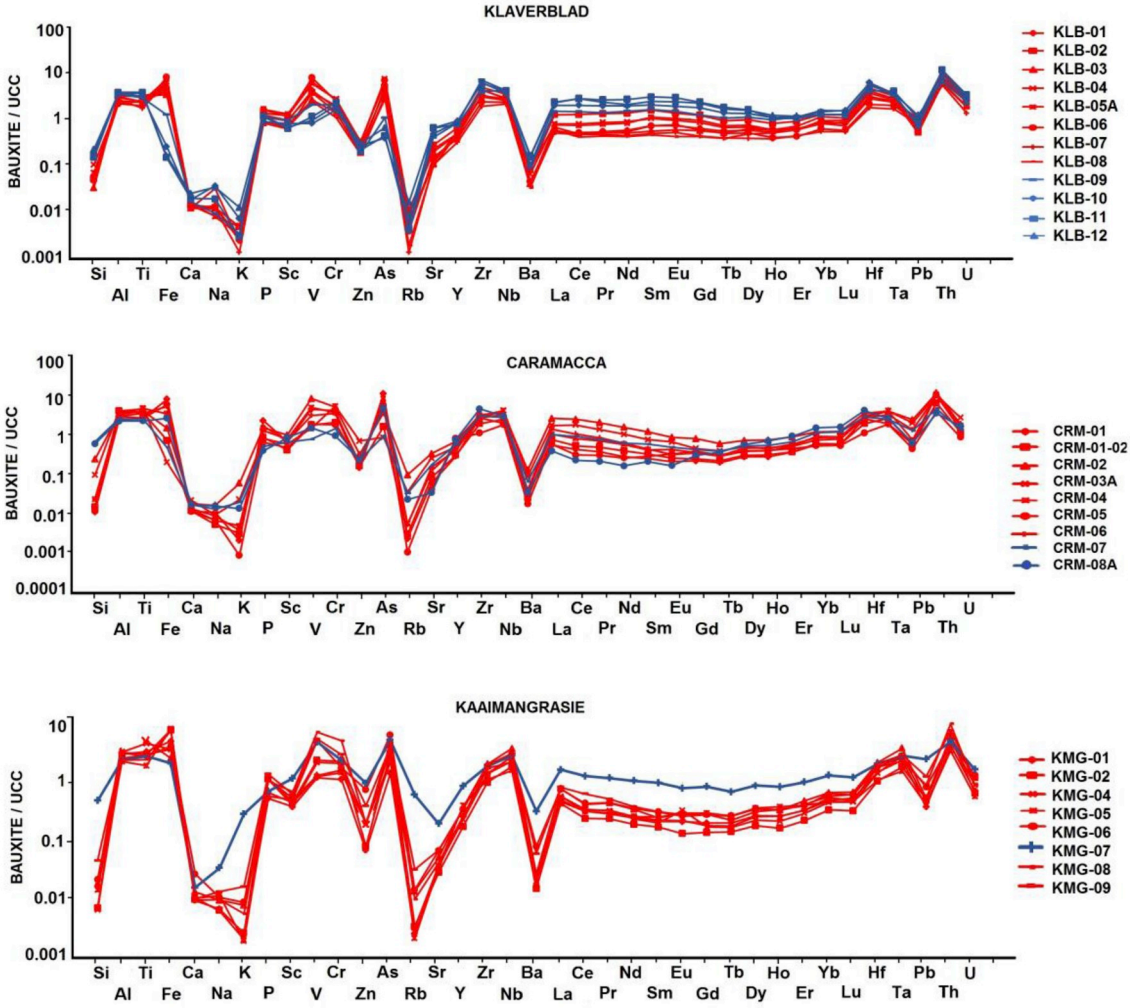


**Fig. 16.** Upper-continental-crust (UCC) normalized element distributions in the studied weathering profiles. Samples indicated in red have < 5 wt% $SiO_2$, while those in blue contain > 5 wt% $SiO_2$. (For interpretation of the references to color in this figure legend, the reader is referred to the Web version of this article.)

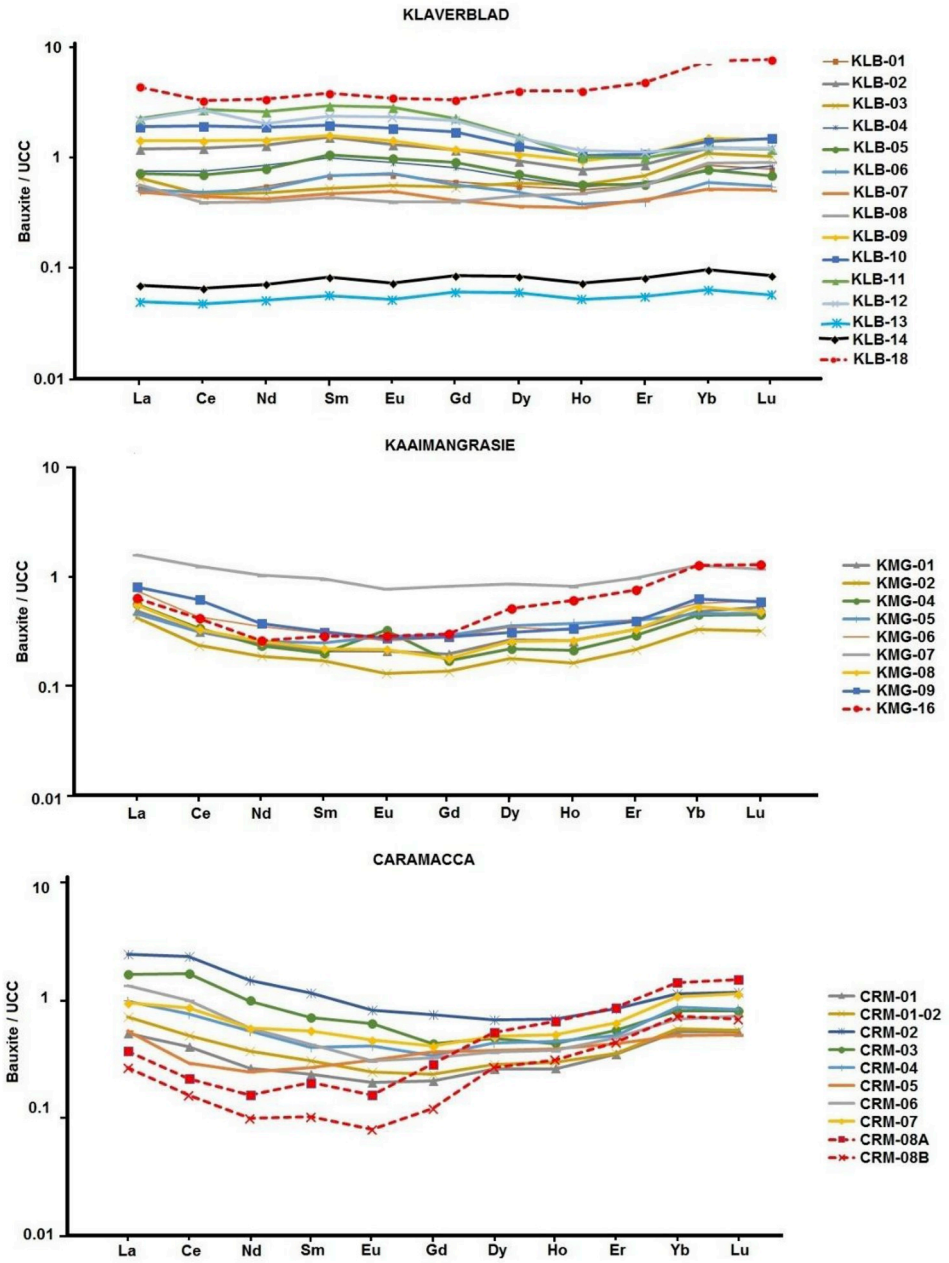


**Fig. 17.** Comparison of UCC-normalized REE patterns of bauxite and underlying saprolitic clay layers (red dotted lines) layers for the Successor deposits. Note the disparity of trends for the saprolitic clays at each location and the anomalously low REE concentrations in the earthy bauxites of Klaverblad (supplementary samples KLB-13 and KLB-14). (For interpretation of the references to color in this figure legend, the reader is referred to the Web version of this article.)

weathering history). Deviating ratios of immobile elements in the CRM kaolin (e.g. relatively low Th/Nb, Cr/Hf) confirm this.

*4.2.4. Provenance of the sediment precursor(s)*

Petrographic observations indicate that the textural diversity of zircon grains in the three Successor deposits could be due to sediment provenance, either from different sources or from a single lithology containing a heterogeneous zircon population. Previous research revealed that the heavy mineral fraction of the Lelydorp II, Lelydorp III and Onoribo II deposits consist for up to 75% of zircon and contains lesser amounts of staurolite, tourmaline and other minerals such as rutile, kyanite, sillimanite and andalusite (Krook, 1969a), while those of the Moengo Hill (MRJ district) chiefly consist of staurolite together with tourmaline, andalusite, kyanite, rutile, anatase and zircon (Van Kersen, 1956). These differences in the heavy mineral fraction clearly reflect differences in provenance with those of the POL district, pointing to derivation from medium to high-grade aluminous metamorphic rock types.

The trace-element signatures also provide indications as to the provenance of the sediments on which the Successor bauxites developed. Ratios of elements that remain immobile during the weathering process may serve to identify chemical properties of the sediment precursor, which may in turn be used to identify the rock type in the hinterland from which it was derived by erosion. Complicating factors are possible effects from sorting/fractionation of the various possible mineral hosts of the elements during riverine transport and deposition. For example, preferential accumulation of zircon in a sediment would enhance the concentrations elements such as Zr, Hf, HREE and Th relative to immobile elements that are incorporated in other mineral hosts (e.g., Nb, Ta).

Despite obvious mobility of many of the elements analyzed and other limitations, several observations can be made. The KLB precursor

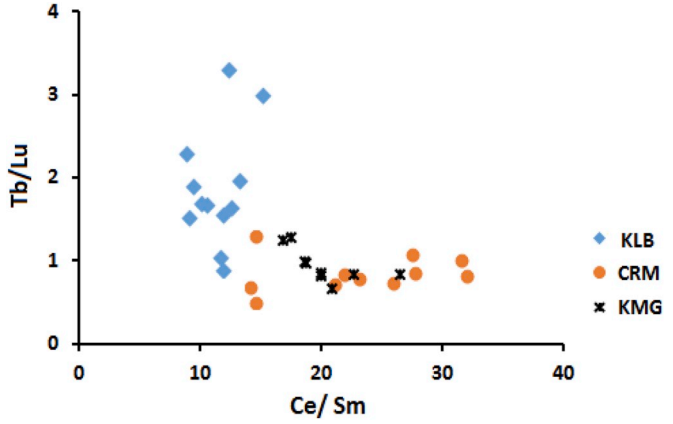


**Fig. 18.** Ce/Sm vs. Tb/Lu ratios of the Successor bauxites, illustrating a chemically distinct trace-element signature of the Klaverblad (KLB) deposit. See text for discussion.

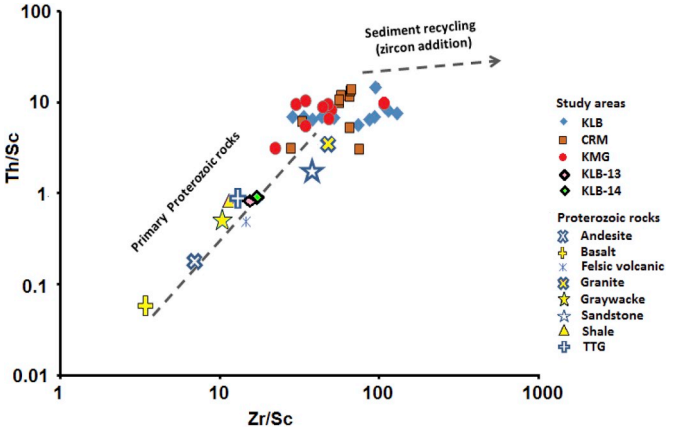


**Fig. 19.** Zr/Sc vs. Th/Sc ratios of the Successor bauxites, compared with average ratios of various Proterozoic rock types (Condie, 1993). See text for discussion.

is chemically distinct from that of the two other Successor deposits, as is illustrated by the Ce/Sm-Tb/Lu plot of Fig. 18. As this difference is difficult to explain by weathering effects, the KLB bauxite must have formed on a different sediment. In view of its location (next to the Suriname River), it was probably derived from another source than the sediments of the more remote Kaaimangrasie and Caramacca deposits (closer to the Commewijne River), which may have had a separate, common source (Fig. 3a).

Fig. 19 compares Zr/Sc and Th/Sc ratios of the Successor bauxites with the chemical signatures of various lithologies, based on average compositions of Proterozoic rock types (Condie, 1993). The bauxites plot at the high end of the trend for Proterozoic rocks, close to the compositions of granite and sandstone that are present in the Surinamese hinterland. However, the source rock of the precursor sediment may have had lower Zr/Sc and Th/Sc ratios and coincide with another rock type further down the trend.

Firstly, because immobility of Sc is questionable, and secondly because sediment recycling may have promoted the accumulation of Zr and/or Th-bearing minerals, yielding higher Zr/Sc and Th/Sc ratios of the bulk sediment. Interestingly, two KLB supplementary samples (earthy bauxites KLB-13, KLB-14) plot close to average Proterozoic shale, felsic volcanics, TTG and greywacke, suggesting that these samples possibly had a precursor with a different lithology. The bauxites show a horizontal trend (most obvious in the KLB samples), which is consistent with zircon accumulation due to sediment recycling (cf., McLennan et al., 1993), in agreement with the abundance of this mineral in the Successor deposits. Trace-element data on the large lithological variety of crystalline basement rocks in Suriname's interior are required to establish the sources of the siliciclastic sedimentary precursors of the coastal-plain bauxite in detail.

## 5. Summary and conclusions

- Vertical compositional profiles, studied in selected coastal-plain deposits in Suriname, revealed that major-element variations within the bauxite sequences mainly reflect distributions of secondary minerals that originated through weathering of terrigenous clastic sediments. Apart from showing classical relationships between mineralogy and chemistry of lateritic bauxites (high $SiO_2$-contents in kaolinite-rich saprolite, maximum $Al_2O_3$ -contents in gibbsite-dominated bauxite layers and highest $Fe_2O_3$-contents in goethite and hematite-rich duricrust), there is considerable compositional variability beyond the effects of leaching and residual accumulation, due to heterogeneity in the original sediment stratigraphy. Bauxite reworking and polycyclic bauxitization have added to the lithofacies complexity in the studied deposits. The upper sections of the Lelydorp-1, Kankantrie (Noord) and Para (Noord) deposits show evidence for resilication by downward percolating silica-bearing fluids, derived from the sedimentary overburden.

- Evidence from the investigated profiles of the Successor deposits indicates that (re-)distributions of many trace elements, particularly HFSE and REE, are mainly controlled by the nature and abundances of heavy minerals in the precursor sediments, and their stability during weathering. Patterns of relatively immobile elements largely reflect abundances of zircon and other weathering-resistant heavy minerals. In contrast, some of the trends also suggest mobility, specifically for LREE, presumably due to breakdown of their original mineral host(s).

- The trace-element signatures of the Successor deposits point to heterogeneity of precursor sediments on a small spatial scale, reflecting variations in provenance or the depositional regime of the local fluviatile environment. The evidence from trace elements and heavy minerals suggests that the coastal-plain bauxites mostly developed on Tertiary terrigenous sediments that are strongly heterogenous, largely due to their predominant origin as erosion products from a diversity of Proterozoic igneous and metamorphic rocks in Suriname's interior. Minor contributions from basement rocks may locally have played a role as well. Conspicuous differences in trace-element signatures (e.g., Ce/Sm and Tb/Lu ratios) between Klaverblad and the other two Successor deposits (Caramacca and Kaaimangrasie) demonstrate the potential variability of precursor sediments and their riverine supply in the coastal-plain bauxites.

- According to field relationships and the trace-element data of the Successor deposits, there is no obvious genetic relationship between bauxite and underlying kaolinitic clay, neither in a uniform weathering profile nor in a scenario wherein bauxite formed on a parent of kaolinitic clay. The presence of kaolinite-rich layers in the coastal-plain bauxite deposits is probably largely controlled by original intercalations of clayey material in the original stratigraphy, although a secondary origin, associated with bauxite formation, cannot always be excluded and should be explored in each individual case.

## Acknowledgements

The authors would like to thank Tilly Bouten, Helen de Waard and Anita van Leeuwen-Tolboom for help with analytical work at Utrecht University. They are also grateful to Pieter Vroon for generously providing access to the laboratory facilities at the VU University, Amsterdam. The Bauxite Institute of Suriname and Suralco kindly provided major-element data and samples from exploration drilling campaigns. This manuscript benefitted significantly from critical and constructive comments of three anonymous reviewers. Research was funded by a grant (SEMIF-11-14) from the Suriname Environmental and Mining Foundation.

## Appendix A. Supplementary data

Supplementary data to this article can be found online at https://doi.org/10.1016/j.jsames.2018.10.010.

## References


Abendini, A., Calagari, A., 2014. REE geochemical characteristics of titanium-rich bauxites; the Permian Kanigorgeh horizon, NW Iran. Turk. J. Earth Sci. 23, 513–5132.

Ahmadnejad, F., Zamanian, H., Taghipour, B., Zarasvandi, A., Buccione, R., Salamab Ellahi, S., 2017. Mineralogical and geochemical evolution of the Bidgol bauxite deposit, Zagros Mountain Belt, Iran: implications for ore genesis, rare earth elements fractionation and parental affinity. Ore Geol. Rev. 86, 755–783.

Aleva, G., 1965. The buried bauxite deposits of Onverdacht, Surinam, South America. Geol. Mijnbouw 44, 45–58.

Aleva, G., 1979. Bauxitic and other duricrusts in Surinam: a review. Geol. Mijnbouw 58, 321–336.

Aleva, G., 1981. Essential differences between the bauxite deposits along the southern and northern edges of the Guiana Shield, South America. Econ. Geol. 76, 1142–1152.

Aleva, G., Wong, Th, 1998. The history of bauxite exploration and mining in Suriname. In: The History of Earth Sciences in Suriname. Royal Netherlands Academy of Arts and Sciences, and Netherlands Institute of Applied Geoscience, TNO, pp. 275–310.

Aleva, G., Coutinho, H., Haug, G., Janssen, J., Krook, L., 1969. Some sections through the bauxite belt of the Zanderij-Onverdacht-Lelydorp Area, Suriname. Verh. het K. Ned. Geol. Mijnbouwkd. Genoot. 27, 85–88.

Anand, R., Gilkes, R., 1984. Weathering of ilmenite in a lateritic palid zone. Clay Clay Miner. 32 (5), 363–374.

Bakker, J., Kiel, H., Müller, H., 1953. Bauxite and sedimentation phases in the Northern part of Surinam (Netherlands Guiana). Geol. Mijnbouw 15, 215–226.

Bárdossy, G., Aleva, G., 1990. Lateritic Bauxites. Developments in Economic Geology, vol. 27. Elsevier Science Publishing, pp. 569.

BHP Billiton Suriname, 2004. Feasibility Study Successor Mines Project 2 of 3. pp. 1–7 section 5.

Bleackley, D., 1964. Bauxites and laterites of British Guiana. Geol. Surv. Br. Guiana Bull. 34.

Bogatyrev, B., Zhukov, V., Tsekhovsky, Y., 2009. Formation conditions and regularities of the distribution of large and superlarge bauxite deposits. Lithol. Miner. Resour. 44 (2), 135–151.

Boulangé, B., 1984. Les formations bauxitiques latéritiques de Côte d'Ivoire. ORSTOM, Paris. Trav. Doc. 175, 314.

Carvalho, A., Boulangé, B., Melfi, A., Lucas, Y. (Eds.), 1997. Brazilian Bauxites, USP. FAPESP, Paris, pp. 331 ORSTOM.

Chan, M., Potter, S., Bowen, B., Parry, W., Barge, L., Seiler, W., Petersen, E., Bowman, J., 2012. In: Grotzinger, J., Milliken, R. (Eds.), Characteristics of Terrestrial Ferric Oxide Concretions and Implications for Mars, Sedimentary Geology of Mars.

Chardon, D., Chevillote, V., Beauvais, A., Grandin, G., Boulangé, B., 2006. Planation, bauxites and epeirogeny: one or two paleosurfaces on the west african margin. Geomorphology 82, 273–282.

Condie, K., 1993. Chemical composition and evolution of the upper continental crust: contrasting results from surface samples and shales. Chem. Geol. 104, 1–37.

Cornu, S., Lucas, Y., Lebon, E., Ambrosi, J., Luizão, Rouiller, Bonnay, M., Neal, C., 1999. Evidence of titanium mobility in soil profiles. Geoderma 91 (3–4), 281–295.

Costa, M.L., Cruz, G.S., Almeida, H.D.F., Poellmann, H., 2014. On the geology, mineralogy and geochemistry of the bauxite-bearing regolith in the lower Amazon basin: evidence of genetic relationships. J. Geochem. Explor. 146, 58–74.

Delvigne, J., 1998. Atlas of Micromorphology of Mineral Alteration and Weathering. Mineral Association of Canada, pp. 509.

Dennen, W.H., Norton, H.A., 1977. Geology and geochemistry of bauxite deposits in the lower Amazon basin. Econ. Geol. 72, 82–89.

Diko, L., Vervoort, A., Vergauwen, I., 2001. Geostatistical modelling of lateritic bauxite orebodies in Suriname: effect of the vertical dimension. J. Geochem. Explor. 73, 131–153.

Doeve, G., Groeneveld Meijer, W., 1963. Bauxite deposits of British Guiana and Suriname in relation to underlying unconsolidated sediments suggesting two-step origin. Econ. Geol. 58, 1060–1062.

Goldschmidt, V., 1937. The principles of distribution of chemical elements in minerals and rocks. J. Chem. Soc. A 655–673 London.

Goldschmidt, V., 1954. Geochemistry. Clarendon press, Oxford, pp. 730.

Gow, N., Lozej, G., 1993. Bauxite. In: In: Sheaham, P., Cherry, M. (Eds.), Ore Deposit Models. Journal of the Geological Association of Canada, Geoscience Canada Reprint, vol. 20. pp. 9–16 1.

Grey, I., Reid, A., 1975. The structure of pseudorutile and its role in the natural alteration of ilmenite. Am. Mineral. 60, 898–906.

Grubb, P., 1979. Genesis of bauxite deposits in the Lower Amazon Basin and Guiana Coastal Plain. Econ. Geol. 74, 735–750.

Huang, W., Keller, W., 1972. Geochemical mechanisms for the dissolution, transport, and deposition of aluminium in the zone of weathering. Clay Clay Miner. 20, 69–74.

Janssen, J., 1970. Preliminary Report on the Coermotibo Exploration. Internal Report of Suralco L.L.C, Paramaribo, Suriname. pp. 1–8.

Janssen, J., 1979. Bauxite and Laterite Hard Caps in Suriname. Unpublished internal report Grassalco, pp. 1–12.

King, L.C., Hobday, D.K., Mellody, M., 1964. Cyclic Denudation in Surinam. Internal Report Geologische Mijnbouwkundige Dienst Suriname, Paramaribo. pp. 1–12.

Kisoensingh, M., 2009. Description and Classification of the Klaverblad, Kaaimangrasie, Caramacca Deposit, District of Commewijne, Suriname. Anton de Kom University of Suriname, pp. 1–60 Unpublished BSc. thesis.

Krook, L., 1969a. Investigations on the mineralogical composition of the Tertairy and Quaternary sands in northern Suriname. In: Proc.7th Guiana. Geol.Conf., Paramaribo, 1966. Verhandelingen Van Het Koninklijk Nederlands Geologisch, Mijnbouwkundig Genootschap, vol. 27. pp. 89–100.

Krook, L., 1969b. The origin of bauxite in the coastal plain of Surinam and Guyana. Mededelingen Geologisch Mijnbouwkundige Dienst 20, 173–180.

Krook, L., 1979. Sediment Petrographical Studies in Northern Suriname, Doctoral Thesis. Free University of Amsterdam, pp. 155.

Kroonenberg, S., De Roever, E., Fraga, L., Reis, N., Faraco, M., Lafon, J., Cordani, U., Wong, Th, 2016. Paleoproterozoic evolution of the Guiana Shield in Suriname: a revised model. Netherlands Journal of Geoscience, Geologie en Mijnbouw 95 (4), 491–522.

Laskou, M., Economou-Eliopoulos, M., 2007. The role of microorganisms on the mineralogical and geochemical characteristics of the Parnassos-Ghiona bauxite deposits, Greece. J. Geochem. Explor. 93, 67–77.

Laveuf, C., Cornu, S., 2009. A review on the potentially rare earth elements to trace pedogenetic processes. Geoderma 154, 1–12.

Lee, M., Parkinson, G., 1999. Growth rates of gibbsite single crystals determined using in situ optical microscopy. J. Cryst. Growth 198, 270–274.

Leonard, J., 1984. Bauxite, Proceedings of the 1984 Bauxite Symposium. Society of Mining Engineers AIME, Los Angeles, California, pp. 387–407 February 27-March 1.

Ling, K.-Y., Zhu, X.-Q., Tang, H.-S., Shi-Xin Li, S.-X., 2017. Importance of hydrogeological conditions during formation of the karstic bauxite deposits, Central Guizhou Province, Southwest China: a case study at Lindai deposit. Ore Geol. Rev. 82, 198–216.

Ling, K.-Y., Zhu, X.-Q., Tang, H.-S., Du, S.-J., Ga, J., 2018. Geology and geochemistry of the Xiaoshanba bauxite deposit, Central Guizhou Province, SW China: implications for the behavior of trace and rare earth elements. J. Geochem. Explor. 190, 170–186.

Logemerac, V., 1969. The distribution of rare earths and other minor elements in Surinam bauxite and laterite and in the red mud obtained from them. Verh. het K. Ned. Geol. Mijnbouwkd. Genoot. 27, 155–162.

Mateus, A., Oliveira, F., Varajao, A., Soares, C., 2017. Genesis of soils from bauxite in South eastern Brazil: resilicationn as a soil-forming process. Rev. Bras. Ciência do Solo 41, e01060507 [online] {cited 05-09-2018}.

McLennan, S., Hemming, S., McDaniel, D., Hanson, G., 1993. Geochemical approach to sedimentation, provenance, tectonics. In: In: Johnsson, M., Basu, A. (Eds.), Processes Controlling the Composition of Clastic Sediments: Boulder, vol. 284. Geolocial Society of America special paper, Coldorado, pp. 21–40.

Monsels, D., 2004. New Data Related to the Origin of the Coermotibo Deepseated Deposit, District of Marowijne. Unpublished BSc thesis, Anton de Kom University, pp. 38pp.

Monsels, D., 2016. Bauxite deposits in Suriname: geological context and resource development. Neth. J. Geosci. 95, 405–418.

Monsels, D., Van Bergen, M., 2017. Bauxite formation on Proterozoic bedrock of Suriname. J. Geochem. Explor. 180, 71–90.

Monsels, D., Van Bergen, M., Mason, P., 2018. Trace element analysis of bauxite using laser ablation inductively coupled plasma mass spectrometry on lithium borate glass beads. Geostand. Geoanal. Res. 42 (2), 239–251.

Moses, J., Michell, W., 1963. Bauxite deposits of British Guiana and Surinam in relation to underlying unconsolidated sediments suggesting two-step origin. Econ. Geol. 58 (2), 250–262.

Nesbitt, H., Young, G., 1982. Early Proterozoic climates and plate motions inferred from major element chemistry of lutites. Nature 299, 715–717.

Oliveira, S.B., Costa, M.L., Prazeres Filho, H., 2016. The lateritic bauxite deposit of Rondon do Pará: a new giant deposit in the Amazon region, Northern Brazil. Econ. Geol. 111, 1277–1290.

Patterson, S., Kurtz, H., Olson, J., Neeley, C., 1986. World Bauxite Resources; Geology and Resources of Aluminum. U.S. Geological Survey Professional Paper, 1076-B. United States Government Printing Office, Washinghton, pp. 158.

Pollack, H., 1983. Land surfaces and lateritization in Suriname. In: Melfi, A., Carvalho, A. (Eds.), Proc. 2nd Int. Sem. On Lateritisation Processes, 1982, São Paulo, Brazil, pp. 295–308.

Putthapiban, P., Hongsresawat, S., 2007. Formation of Hollow Concretions in Northeastern Thailand. Advances in Geosciences, 13, Solid Earth. World Scientific Publishing, Singapore, pp. 13–22.

Rudnick, R., Gao, S., 2004. Composition of the continental crust. In: Holland, H., Turekian, K. (Eds.), Treatise on Geochemistry. vol. 3. Elsevier, Amsterdam, pp. 1–64.

Schaetz, R., Anderson, S., 2009. Soils; Genesis and Geomorphology. Cambridge University press, Cambridge, pp. 817.

Schellman, W., 1986. A new definition of laterite. On the geochemistry of laterites. Chem. Erde 45, 39–43.

Schellmann, W., 1983. A new definition of laterite. Natural resources and development, Hannover/Tubingen 18, 7–12.

Schwertmann, U., 1991. Solubility and dissolution of iron oxides. Plant Soil 130, 1–25.

SPS & OAS (Stichting Planbureau Suriname & Organisation of American States), 1988. Suriname Planatlas. SPS/OAS, Washington, D.C, pp. 48.

Tardy, Y., 1997. Petrology of Laterites and Tropical Soils. A.A. Balkema publishers, Rotterdam, Brookfield, pp. 377.

Tardy, Y., Nahon, H., 1985. Geochemistry of laterites, stability of Al-goethite, Al-hematite, and Fe3+-kaolinite in bauxites and ferricretes: an approach to the mechanism of concretion formation. Am. J. Sci. 285, 865–903.

Taylor, G., Eggleton, R., 2008. Genesis of pisolites and of the Weipa Bauxite deposit, northern Australia. Aust. J. Earth Sci. 55, 87–103.

Théveniaut, H., Freyssinet, Ph, 2002. Timing of lateritization on the Guiana Shield:

synthesis of paleomagnetic results from French Guiana and Suriname. Palaeography, Palaeoclimatology, Palaeoecology 178, 91–117 Elsevier.
Valeton, I., 1971. Tubular fossils in the bauxites and the underlying sediments of Surinam and Guyana. Geol. Mijnbouw 50 (6), 733–741.
Valeton, I., 1972. Bauxites, vol. 1. Elsevier, Development in Soil Sciences, pp. 213.
Valeton, I., 1979. Tubular fossils in the bauxites and underlying sediments of Surinam and Guyana. Geol. Mijnbouw 50 (6), 733–741.
Valeton, I., 1983. Paleoenvironment of lateritic bauxites with vertical and lateral differentiation. Geological Society 11, 77–90 London, Special Publications.
Van der Hammen, T., 1969. Introduction and short outline of the history of the 'younger' areas of the Guiana's. Verh. het K. Ned. Geol. Mijnbouwkd. Genoot. 27, 9–12.
Van der Hammen, T., Wijmstra, T., 1964. A palynological study on the tertiary and the upper cretaceous of british Guiana. Leidse Geol. Meded. 30, 183–241.
Van der Laan, S., 1998. Mineralogy and Textures of Suriname Bauxites: Report Prepared for Billiton. Hoogovens Research and Development, IJmuiden, pp. 1–15.
Van Kersen, J., 1956. Bauxite deposits in Suriname and demerara (british Guiana), thesis leiden; also published in Leidse Geologische. Mededelingen 21, 247–375.
Velde, B., Meunier, A., 2008. The Origin of Clay Minerals in Soils and Weathered Rocks. Springer-Verlag Berlin Heidelberg, pp. 378.
Wang, H., Bigham, J., Tuovinen, O., 2007. Oxidation of marcasite and pyrite by iron-ozidizing bacteria and archaea. Hydrometallurgy 88 (1–4), 127–131.
Wei, X., Ji, H., Wang, S., Chu, H., Song, C., 2014. The formation of representative lateritic weathering covers in south –central Guangxi (Southern China). Catena 118, 55–72.
Wijmstra, T., Van der Hammen, T., 1964. Palynological data on the age of the bauxite in british Guiana and surinam. Geol. Mijnbouw 44, 143.
Wong, Th, 1989. Revision of the stratigraphy of the Coastal plain of Suriname. Natuurwetenschappelijke studiekring voor Suriname en de Nederlandse Antillen 125 (Amsterdam).
Wong, Th, Krook, L., Zonneveld, J., 1998. Investigations in the coastal plain and offshore area of Suriname. In: Wong, Th, de Vletter, D., Krook, L., Zonneveld, I., Van Loon, A. (Eds.), The History of Earth Sciences in Suriname. Royal Netherlands Academy of Arts and Sciences, and Netherlands Institute of Applied Geoscience, TNO, pp. 73–100.
Wong, Th, de Kramer, R., de Boer, P., Langereis, C., Sew-A-Tjon, J., 2009. The influence of sea-level changes on tropical coastal lowlands; the Pleistocene Coropina Formation, Suriname. Sediment. Geol. 216, 125–137.
Zhu, C., Veblen, D., Blum, A., Chipera, S., 2006. Naturally weathered feldspar surfaces in the Navajo sandstone aquifer black mesa, Arizona; electron microscopic characterization. Geochem. Cosmochim. Acta 70, 4600–4616.
Zhu, B., Fang, B., Li, X., 2010. Dehydration reactions and kinetic parameters of gibbsite. Ceram. Int. 36, 2493–2498.